

Ethane in planetary and cometary atmospheres: Transmittance and fluorescence models of the ν_7 band at 3.3 μm

G. L. Villanueva,^{1,2} M. J. Mumma,¹ and K. Magee-Sauer³

Received 23 December 2010; revised 21 April 2011; accepted 31 May 2011; published 30 August 2011.

[1] Ethane and other hydrocarbon gases have strong rovibrational transitions in the 3.3 μm spectral region owing to C-H, CH₂, and CH₃ vibrational modes, making this spectral region prime for searching possible biomarker gases in extraterrestrial atmospheres (e.g., Mars, exoplanets) and organic molecules in comets. However, removing ethane spectral signatures from high-resolution terrestrial transmittance spectra has been imperfect because existing quantum mechanical models have been unable to reproduce the observed spectra with sufficient accuracy. To redress this problem, we constructed a line-by-line model for the ν_7 band of ethane (C₂H₆) and applied it to compute telluric transmittances and cometary fluorescence efficiencies. Our model considers accurate spectral parameters, vibration-rotation interactions, and a functional characterization of the torsional hot band. We integrated the new band model into an advanced radiative transfer code for synthesizing the terrestrial atmosphere (LBLRTM), achieving excellent agreement with transmittance data recorded against Mars using three different instruments located in the Northern and Southern hemispheres. The retrieved ethane abundances demonstrate the strong hemispheric asymmetry noted in prior surveys of volatile hydrocarbons. We also retrieved sensitive limits for the abundance of ethane on Mars. The most critical validation of the model was obtained by comparing simulations of C₂H₆ fluorescent emission with spectra of three hydrocarbon-rich comets: C/2004 Q2 (Machholz), 8P/Tuttle, and C/2007 W1 (Boattini). The new model accurately describes the complex emission morphology of the ν_7 band at low rotational temperatures and greatly increases the confidence of the retrieved production rates (and rotational temperatures) with respect to previously available fluorescence models.

Citation: Villanueva, G. L., M. J. Mumma, and K. Magee-Sauer (2011), Ethane in planetary and cometary atmospheres: Transmittance and fluorescence models of the ν_7 band at 3.3 μm , *J. Geophys. Res.*, 116, E08012, doi:10.1029/2010JE003794.

1. Introduction

[2] Ground-based infrared astronomy is a powerful tool for characterizing molecular compositions of cometary and planetary atmospheres. In the 1990s, advances in infrared detectors enabled scientists to study bright infrared lines in comets and planets and to characterize their chemical compositions with unprecedented sensitivity. In 1999, commissioning of the first cross-dispersed infrared spectrometer at a large aperture telescope (Near-Infrared Echelle Spectrograph (NIRSPEC) for the Keck II telescope [McLean *et al.*, 1998]) closed the century that saw infrared spectroscopy transition from single-element thermopiles behind low-resolution spectrographs to million-pixel detector arrays behind high-resolution spectrometers that span the entire 1–5 μm wave-

length range. Similar instruments followed quickly at other giant telescopes, together driving a revolution in molecular astronomy. The higher sensitivities and improved spectral resolution of these instruments have highlighted the limitations of current models for analyzing spectra acquired with them, and have revealed ancillary issues introduced by incomplete and/or incorrect molecular parameters. The latter problem is especially acute in the important near-infrared spectral region, where all aliphatic and aromatic hydrocarbons have infrared-active vibrational modes.

[3] Hydrocarbon gases have strong rovibrational transitions in the 3.3 μm spectral region owing to C-H, CH₂, and CH₃ vibrational modes, making this spectral region prime for searching possible biomarker gases in extraterrestrial atmospheres (e.g., Mars, exoplanets) and organic molecules in comets. For example, ethane has strong ν_7 and ν_5 fundamental bands with origins at wavelengths (frequencies) near 3.35 μm (2985 cm^{-1}) and 3.45 μm (2896 cm^{-1}), respectively. The discovery of abundant ethane in comet C/1996 B2 (Hyakutake) [Mumma *et al.*, 1996], as well as its detection in every comet sampled since then [DiSanti and Mumma, 2008; Mumma and Charnley, 2011, and references therein], created a need for accurate models of solar-pumped fluorescence for

¹Solar System Exploration Division, NASA Goddard Space Flight Center, Greenbelt, Maryland, USA.

²Department of Physics, Catholic University of America, Washington, DC, USA.

³Department of Physics and Astronomy, Rowan University, Glassboro, New Jersey, USA.

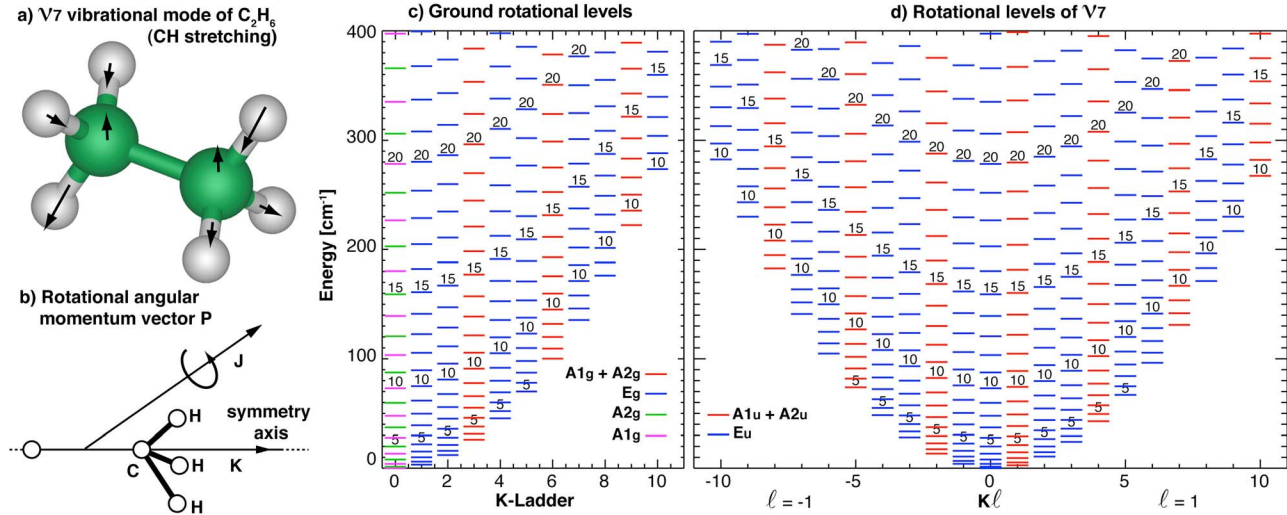


Figure 1. Rotational structure of ground and ν_7 vibrational levels of C₂H₆. (a) Relative motions of atoms of C₂H₆ associated with ν_7 vibrational mode. (b) Rotational angular momentum (related to J quantum number) and its projection along the symmetry axis (related to K quantum number). (c, d) Rotational levels for ground and ν_7 vibrational states, respectively, with symmetries indicated by different trace types.

these two vibrational bands. A simple initial model for the four Q branches seen in Hyakutake was soon extended to account for the increased number of Q branches observed in C/1995 O1 (Hale-Bopp) [Dello Russo *et al.*, 2001]. The rapid increase in power of cross-dispersed and high-resolution infrared spectrometers (NIRSPEC in 1999, Cryogenic High-Resolution Infrared Echelle Spectrograph (CRIRES) in 2005) soon revealed even more spectral lines of ethane ν_7 [Mumma *et al.*, 2001; Dello Russo *et al.*, 2006] and stimulated the first systematic study of ν_5 [Radeva *et al.*, 2011] in comets. However, the incomplete or improper accounting of ethane in public spectral databases seriously constrained the accuracy of models for telluric transmission and thus limited the achievable sensitivities for data taken using ground-based telescopes.

[4] In this article, we present a complete quantum mechanical model for the rovibrational ν_7 band of ethane (C₂H₆), using accurate spectral parameters. We next discuss the limitations of molecular databases and models for synthesizing telluric atmospheric transmittance and the solar spectrum, as well as present improved models for this purpose. We then obtain new line-by-line fluorescence efficiencies for ethane in space by coupling the new ν_7 band model with the solar spectrum (including Fraunhofer lines). Finally, we synthesize the terrestrial transmittance spectrum using improved molecular parameters (including ethane ν_7). We illustrate the increases in accuracy and sensitivity achieved by applying these models to ground-based spectra of Mars and comets (C/2004 Q2 (Machholz), 8P/Tuttle, and C/2007 W1 (Boattini)).

2. Ethane Model

[5] HITRAN is a comprehensive database of molecular parameters that is widely used by the spectroscopic community for synthesizing and analyzing spectra of atmospheric gases. The database undergoes regular updates and additions, and its completeness has improved greatly in recent years.

The latest version [Rothman *et al.*, 2009] contains almost 3 million lines from 42 molecules, yet the database is still not sufficient in some spectral regions. Ethane provides a good example. Even though C₂H₆ is present in the terrestrial atmosphere at only trace amounts (0.1–2 ppbv), the lines of its strongest band (ν_7) are prominent in high-resolution atmospheric spectra. The latest HITRAN distribution includes parameters for some Q branches derived by Brown *et al.* [1987] from ATMOS spectra, with later improvements for the PQ_3 subband from Pine and Rinsland [1999]. P and R branch lines are not listed. Here, we present a complete quantum mechanical band model for the ν_7 band, including lines of P , Q , and R branches.

2.1. Rovibrational Structure

[6] For decades, laboratory scientists have extensively studied the rovibrational bands of C₂H₆, but due to the complex morphology of the ethane bands and strong spectral confusion only a limited set of spectroscopic constants have been retrieved. Ethane is composed of two methyl groups in which H atoms of the CH₃ groups are sterically staggered by 60° about the C-C axis of threefold symmetry. The molecule has 12 fundamental vibrations involving C-H and C-C stretching (ν_1 , ν_3 , ν_5 , ν_7 , ν_{10}), deformation of the methyl group (ν_2 , ν_6 , ν_8 , ν_{11}), torsion (ν_4), and bending (ν_9 , ν_{12}). The perpendicular band at 3.3 μm (ν_7) is infrared active and originating by the stretching of the C-H bonds of individual methyl groups (Figure 1a). The characterization of rotational structure in this complex molecule is nontrivial because the ν_7 band is severely perturbed by overtones and combination states (with a low-frequency torsional mode (ν_4) at ~289 cm⁻¹) that are in Fermi or Coriolis resonance with ν_7 [Pine and Lafferty, 1982]. For some K subbands (e.g., RQ_5), the perturbations are so severe that the energy levels cannot be simply described using a standard power series expansion [Pine and Lafferty, 1982].

[7] Description of the energy levels was performed using linear progressions of J , K , and ℓ (where " denotes lower state

Table 1a. Model Parameters: Rotational Constants for the Ground Vibrational State [Pine and Lafferty, 1982]

	Ground State Constants (cm^{-1})
A_0	2.671
B_0	0.6630271
D_{JK}^0	1.09×10^{-5}
D_0^J	2.660×10^{-6}
D_0'	1.0312×10^{-6}

and ' upper state). Considering that C_2H_6 is a prolate symmetric top molecule, the quantum numbers J and K , respectively, indicate the total angular momentum of the molecule and its projection onto the symmetry axis; thus, $K \leq J$ (Figure 1b). For the ground vibrational state (Figure 1c), we applied the constants compiled by Pine and Lafferty [1982] (summarized in Table 1a) in the form of

$$\begin{aligned} E''(J'', K'') = & (A - B)K''^2 + BJ''(J'' + 1) - D_J J''^2(J'' + 1)^2 \\ & - D_{JK} J''(J'' + 1)K''^2 - D_K K''^4. \end{aligned} \quad (1)$$

We have had success using this simple progression for most sets of lines; however, we have encountered problems when trying to match the P , R , and Q lines of $K\ell''=0$ ($\Delta K=1$). This difficulty indicates the limitations of this simple approximation, and a more detailed and complete model of the energies for the ground state is required to correctly model fundamental bands of ethane. We have provisionally circumvented this problem by defining a different set of upper-state rotational constants for $\Delta J=0$ and $\Delta J \neq 0$ for $K\ell'=1$ (Table 1b).

[8] For the upper state, Goldman *et al.* [1989] obtained a relatively accurate set of rotational constants for each K ladder using high-resolution spectra recorded by Cole *et al.* [1980] and Pine and Lafferty [1982]. As described by Goldman *et al.* [1989], this power series approximation of J and K does not fully characterize the complexity of the ν_7 band, but it does achieve a reasonable precision of 0.004–0.010 cm^{-1} in frequency [Goldman *et al.*, 1989, Table 2] for a limited number of lines. In 1996, Pine and Stone [1996] provided refined rotational constants for a limited set of Q lines of RQ_0 , PQ_3 , and RQ_3 (including splittings by torsional tunneling and A_1 - A_2 doublings). More recently, Harrison *et al.* [2010] have obtained high-resolution line strengths (cross sections) for ethane in the 3 μm region at temperatures between 194 K and 297 K and total pressures from 0.0689 torr to 763.48 torr. Using this data set, we identified 466 lines, which we consolidated with 122 lines reported by Dang-Nhu *et al.* [1984] and 66 observed by Pine and Stone [1996], ultimately deriving rotational constants for 30 K ladders (Tables 1b and 1c) of the ν_7 band of ethane. The upper-state energies are calculated following:

$$\begin{aligned} E'(J', K\ell') = & F'_{K\ell'} + B'_{K\ell'} J'(J'+1) - D'_{K\ell'} J'^2(J'+1)^2 \\ & + H'_{K\ell'} J'^3(J'+1)^3 + T_{K\ell'}(J'), \end{aligned} \quad (2)$$

where the F , B , D , and H coefficients were fitted for each K ladder using the compilation of lines reported previously. We retrieved the third-order coefficient (H) only when the precision of line frequencies was sufficient to quantify this parameter. For some K ladders, we observe strong perturbations that cannot be described using a simple linear progression.

These perturbations were described using the following formula:

$$T_{K\ell'}(J') = P1_{K\ell'} \cdot (J' - P2_{K\ell'}) \cdot \exp(P3_{K\ell'} \cdot |J' - P2_{K\ell'}|), \quad (3)$$

where $P1$, $P2$, and $P3$ are the perturbation coefficients summarized in Table 1c. A representation of these perturbations for RQ_2 is presented in Figure 2. For lines beyond $K\ell' < -8$ and $K\ell' > 10$, we neglect the T and H terms of equation (3), and describe the energy origins (F) and effective rotational constant (B) following Goldman *et al.* [1989] with

$$F' = v_0 - 2(A\zeta)K'\ell' + (A' - B')K'^2 - D'_{KK}K'^4 + \eta'_{KK}K'^3\ell' \quad (4)$$

$$B' = B_0 - D'_{JK}K'^2 + \eta'_{JK}\ell', \quad (5)$$

in which the parameters (see values in Table 1d) were fitted to all identified lines, with the exception of lines accessing $K'=4, 5, 6$, which appear to be especially perturbed.

[9] Using this energy model, we obtained a standard deviation of 0.005 cm^{-1} for 654 lines with quantum numbers: $-8 \leq K\ell' \leq 10$, and $J' \leq 28$ (Figure 2). These solutions do provide good results for the selected lines, but because of the numerous perturbations their validity for higher quanta and

Table 1b. Model Parameters: Rotational Constants for the ν_7 Vibrational State^a

$K\ell'$	Sym	F (cm^{-1})	B (cm^{-1})	$D \times 10^{-6}$ (cm^{-1})	Lines	rms (cm^{-1})
-8	A_s	3120.55085	0.66367616	1.6379	6	0.00083
-8	E_s	3120.57306	0.66354001	1.0500	4	0.00781
-7	E_u	3089.50468	0.66330074	0.7167	15	0.00749
-6	E_u	3062.67031	0.66214093	-2.0388	22	0.00632
-5	A_s	3039.18324	0.66383076	17.2659	19	0.00750
-5	E_s	3039.36507	0.66090799	-4.2371	10	0.00103
-4	E_u	3020.45860	0.66348953	2.1859	25	0.00699
-3	E_s	3005.61858	0.66348639	1.7780	11	0.01241
-3	G_s	3005.63978	0.66329109	1.2006	23	0.00344
-2	A_s	2994.84157	0.66312225	0.9459	14	0.00002
-2	E_s	2994.83990	0.66312201	0.9767	10	0.00005
-1	E_u	2988.09979	0.66303157	0.8945	36	0.00124
0	E_u^b	2985.38894	0.66303542	1.0141	22	0.00155
1	A_u^b	2986.72474	0.66308908	1.0296	31	0.00245
1	A_s^c	2986.72634	0.66289178	0.9789	14	0.00002
1	E_s^c	2986.73272	0.66285832	1.1544	10	0.00004
2	E_s	2992.09430	0.66299073	1.2681	15	0.00241
2	G_s	2992.09721	0.66292818	1.0268	32	0.00644
3	E_s	3001.50382	0.66315921	1.4885	27	0.00776
3	G_s	3001.50571	0.66294774	0.9871	26	0.00428
4	A_s	3014.94266	0.66295652	0.9703	32	0.00111
4	E_s	3014.93730	0.66296202	1.0594	16	0.00047
5	E_u	3032.40473	0.66300958	0.8346	34	0.00127
6	E_u	3053.85189	0.66352169	0.6270	53	0.00565
7	A_u	3079.69389	0.65843003	-4.3470	41	0.00808
8	E_s	3108.98384	0.66162133	0.5372	19	0.00072
8	G_s	3108.98763	0.66150373	0.4632	38	0.00748
9	E_u	3142.50886	0.66190851	0.8715	16	0.00164
10	A_s	3180.03893	0.66210580	1.3212	22	0.00133
10	E_s	3180.03545	0.66215115	1.3664	11	0.00185

^aRotational constants and perturbations were obtained for each K ladder considering equations (2) and (3).

^bFor RQ_0 , limitations in the description of the ground state were circumvented by defining a different set of upper-state rotational constants for $\Delta J \neq 0$.

^cRotational constants for the RQ_0 ($\Delta J=0$) branch were obtained from Pine and Stone [1996].

Table 1c. Model Parameters: Perturbation Coefficients and High-Order Rotational Constants^a

$K\ell'$	Sym	P_1	P_2	P_3	$H \times 10^{-11}$ (cm $^{-1}$)
-7	E_u	0.1760	9.6954	-1.3818	
-6	E_u				-240.7280
-4	E_u	2.8068	21.2584	-1.7843	338.1293
-3	G_s	0.2090	5.9299	-0.9862	
1	A_s				5.2861 ^b
1	E_s				51.1299 ^b
2	G_s	0.4384	23.9358	-1.0348	
3	E_s	0.3688	11.2986	-1.9035	
3	G_s	0.3524	13.5662	-1.7339	
7	A_u	0.0367	15.4387	-0.1476	-253.0972
8	G_s	0.3183	20.7249	-1.3233	
10	A_s	0.0430	16.4071	-1.3051	
10	E_s	0.1812	17.6675	-0.9935	

^aRotational constants and perturbations were obtained for each K ladder considering equations (2) and (3).

^bRotational constants for the RQ_0 ($\Delta J=0$) branch were obtained from Pine and Stone [1996].

weaker spin species is uncertain. The use of individual constants for each K ladder provides a major advance (see spectra in Figure 3), corresponding to a 36-fold improvement with respect to the 0.18 cm $^{-1}$ standard deviation obtained using a single progression, as in equations (4) and (5), with the global factors in Table 1d, and a 50-fold improvement to the 0.25 cm $^{-1}$ standard deviation obtained using the global constants provided by Goldman *et al.* [1989] (see comparison in Figure 2).

2.2. Spin Symmetries and Spin Temperature

[10] The characterization of the unique symmetries in the ethane molecule is particularly confusing, especially because different authors consider different notations depending on the assumed point group model. If internal rotation tunneling is neglected, then the symmetries of the levels can be

Table 1d. Model Parameters: Rotational Constants for $-8 > K > 10^a$

	High-K Constants (cm $^{-1}$)
ν_0	2985.3953
B'	0.66311490
$A\zeta'$	0.34385599
$A'-B'$	2.0208281
D_J'	8.9352×10^{-7}
D_{JK}'	6.8549×10^{-6}
D_K'	-2.0192×10^{-5}
n_J'	-7.82×10^{-5}
nK'	-7.12×10^{-4}

^aFor high K subbands, we fitted the energies of all lines (with the exception of the highly perturbed $K'' = 4, 5, 6$) to the global progression presented in equations (4) and (5).

described with a point group D_{3d} (staggered) model having three spin modifications (A_1, A_2, E) with ‘g’ and ‘u’ notations. In cases where torsional tunneling leads to noticeable splittings, the symmetries are best described with the G^{+}_{36} permutation-inversion group having seven different symmetries ($A_{1s}, A_{4s}, E_{1s}, E_{2s}, E_{3s}, E_{4s}, G_s$). Symmetries of rotational levels in the ground and ν_7 vibrational states are presented in Table 2 for both point groups, including statistical weights (w'' and w'). Because both notations use similar letters (A, E), the reader should be careful not to confuse these definitions when examining previous publications. In this article, we use both notations and distinguish between these definitions by preserving the spin label subscripts (‘g’ and ‘u’ for the D_{3d} model, and ‘s’ for the G^{+}_{36} model). Lines are only permitted between $A \leftrightarrow A$, $E \leftrightarrow E$, and $G \leftrightarrow G$ levels (for both notations), and thus exchange between different spin species is normally considered negligible.

[11] The spin ratios (or equivalent spin temperature) (Figure 4) can be related to the formation conditions of the molecule and, ultimately, be used as a cosmogonical indicator. Unfortunately, little is known about the interconversion of

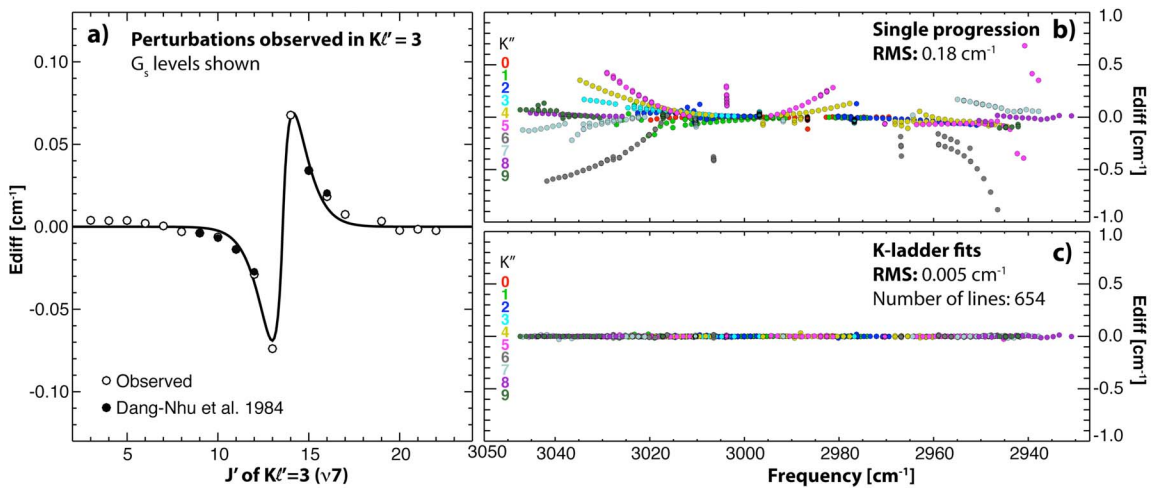


Figure 2. Description of rotational levels of ν_7 vibrational state. (a) Effect of local perturbations on energy distribution of rotational levels. Empirical values were fitted to a quadratic progression and a perturbation function (trace) considering values presented in Tables 1b and 1c. (b) Energy residuals obtained when performing a global fit to rotational lines of ν_7 vibrational level using a single progression for all K ladders. (c) Residuals for 654 lines using individual coefficients for each K ladder (Tables 1b and 1c).

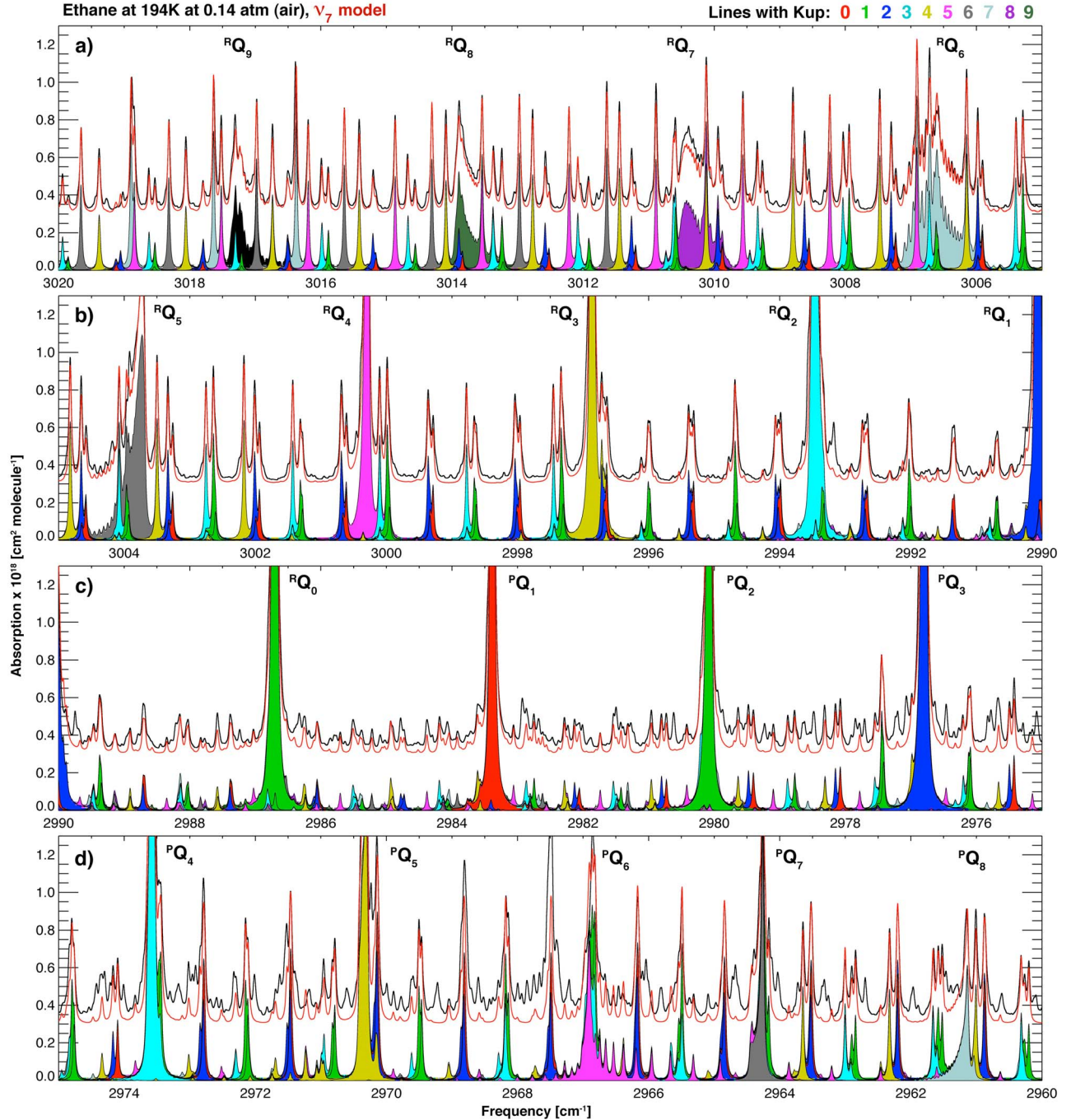


Figure 3. (a–d) Individual K subbands of ν_7 band of ethane compared to absorption cross sections obtained by Harrison *et al.* [2010] for a temperature of 194 K and a pressure of 0.14 atm of synthetic air. Total model (red) and measured (black trace) absorption cross sections have been displaced by 0.3 for clarity purposes.

spin states in molecules with such high-dimensional symmetry. A similar molecule (C_2H_4) was studied by Sun *et al.* [2005], who observed conversions among nuclear spin isomers but no exchange in the inversion symmetry. However, in the case of ethane, its molecular symmetry group does not have a unique element relating to inversion in space, as nicely summarized by Hougen and Oka [2005]. Thus, the relationship between spin ratio at formation and after elapsed times of order billions of years is uncertain; further studies are

required to properly assess this property of the ethane molecule. As shown in Figure 4, the relationship between E_g/A_g becomes equilibrated at very low temperatures (>10 K), much lower than for the curves of H_2O , NH_3 , and CH_4 .

2.3. Line Intensities

[12] The selection rules for the ν_7 band of ethane are: $\Delta J = J' - J'' = +1, 0, -1$; $\Delta K = K' - K'' = \ell' = +1, -1$, and $A \leftrightarrow A$, $E \leftrightarrow E$, $G \leftrightarrow G$. Line intensities S_ν (cm^{-1} (mol cm^{-2}) $^{-1}$)

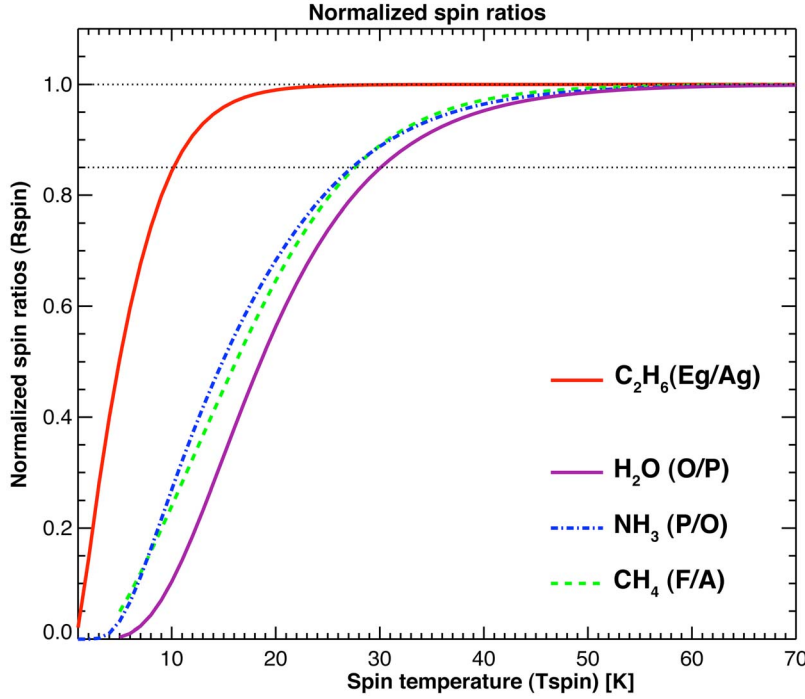


Figure 4. Symmetry ratio of ethane ($A_g = A_{1g} + A_{2g}$ and E_g) considering D_{3d} point group, $E_g/A_g = 5/3$ at equilibrium (eq)) in comparison to water (H_2O , $O/P = 3$ at eq), ammonia (NH_3 , $P/O = 1$ at eq), and methane (CH_4 , $F/A = 9/5$ at eq).

between allowed upper and lower states with $K'' < 20$ and $J'' < 50$ were computed as following:

$$S_\nu(T) = (\nu/\nu_0) S_\nu^0(T) L_{HL}(J'', K'', \Delta J, \Delta K) F_{HW}(J'', K'', \Delta J, \Delta K) \cdot SE(\nu) Pop(E'', w'', T), \quad (6)$$

where ν is the line frequency ($E' - E''$ (cm^{-1})), ν_0 is the band center (cm^{-1}), S_ν^0 is the band intensity (cm^{-1} (mol cm^{-2}) $^{-1}$) (Table 1e), L_{HL} is the Hönl-London factor, F_{HW} is the Herman-Wallis factor, SE is the stimulated emission factor, and Pop is the fractional population of the lower state.

[13] The Hönl-London factor (L_{HL}) for a perpendicular band [Herzberg, 1945, p. 426] (m_L is 4 for $K'' \neq 0$ or 2 for $K'' = 0$) is calculated as:

$$\begin{aligned} \Delta J = 1 \quad L_{HL}(J'', K'', \Delta K) &= \frac{(J'' + 2 + K'' \Delta K)(J'' + 1 + K'', \Delta K)}{m_L(J'' + 1)(2J'' + 1)} \\ \Delta J = 0 \quad L_{HL}(J'', K'', \Delta K) &= \frac{(J'' + 1 + K'' \Delta K)(J'' - K'' \Delta K)}{m_L J''(J'' + 1)} \\ \Delta J = -1 \quad L_{HL}(J'', K'', \Delta K) &= \frac{(J'' - 1 - K'' \Delta K)(J'' - K'' \Delta K)}{m_L J''(2J'' + 1)} \end{aligned} \quad (7)$$

The Herman-Wallis factor (F_{HW}) corrects for vibration-rotation interactions because the effective dipolar operator of a molecule (and thus the intensity of a spectral line) depends not only on the total angular momentum but also on vibrational operators. The Herman-Wallis factor was calculated as:

$$F_{HW}(J'', K'', \Delta J, \Delta K) = \left[1 + \alpha K'' \Delta K + \beta \Delta J \left(J'' + \frac{1}{2} + \frac{\Delta J}{2} \right) + L \right]^2, \quad (8)$$

where α and β are the coefficients presented in Table 1e. Stimulated emission is described with $SE(\nu) = [1 - \exp(-\nu hc/kT)]$, and the relative population as $Pop(w'', E'', T) = w'' \exp(-E'' hc/kT)/Q_R(T)$, where hc/K is the second radiation constant and $Q_R(T)$ the rotational partition function at temperature T [$Q_R(296 \text{ K}) = 51,617$].

[14] The three spectroscopic parameters that describe the intensity of the ν_7 band (S_ν^0 , α , and β) were quantified by Dang-Nhu *et al.* [1984] and Dang-Nhu and Goldman [1987] to be $S_\nu^0(296 \text{ K}) = 349 \pm 4.6 \text{ cm}^{-2} \text{ atm}^{-1}$, $\alpha = 0.0144 \pm 0.0012$, and $\beta = 0$ (assumed). We observe a change in the sign in the second term of the Herman-Wallis equation in Dang-Nhu and Goldman [1987] with respect to Dang-Nhu *et al.* [1984], implying a negative value of $\alpha = -0.0144$, that could be related to a misprint by Dang-Nhu and Goldman [1987]. Using the latest cross sections reported by Harrison *et al.* [2010], we retrieved $\alpha = 0.0096 \pm 0.0020$ and $\beta = -0.0034 \pm 0.0020$. Our value of α is within 2σ of that reported by Dang-Nhu *et al.* [1984].

[15] The accuracy and precision of measurements of the total band intensity (S_ν^0) are directly related to the considered calibration standards and the scheme considered to mitigate for spectral confusion. The latter is particularly crucial for ethane near $3.3 \mu\text{m}$ because multiple fundamental (e.g., ν_7

Table 1e. Model Parameters: Intensity Factors for the ν_7 Band of Ethane

Intensity Parameters	
$S_\nu^0(296 \text{ K}) = 301(24) \text{ (cm}^{-2} \text{ atm}^{-1}\text{)}$	$1.21(10) \times 10^{-17} \text{ [cm}^{-1}/(\text{mol cm}^{-2})]$
α	$0.0096(20)$
β	$-0.0034(20)$
$Q_R(296 \text{ K})$	51,617

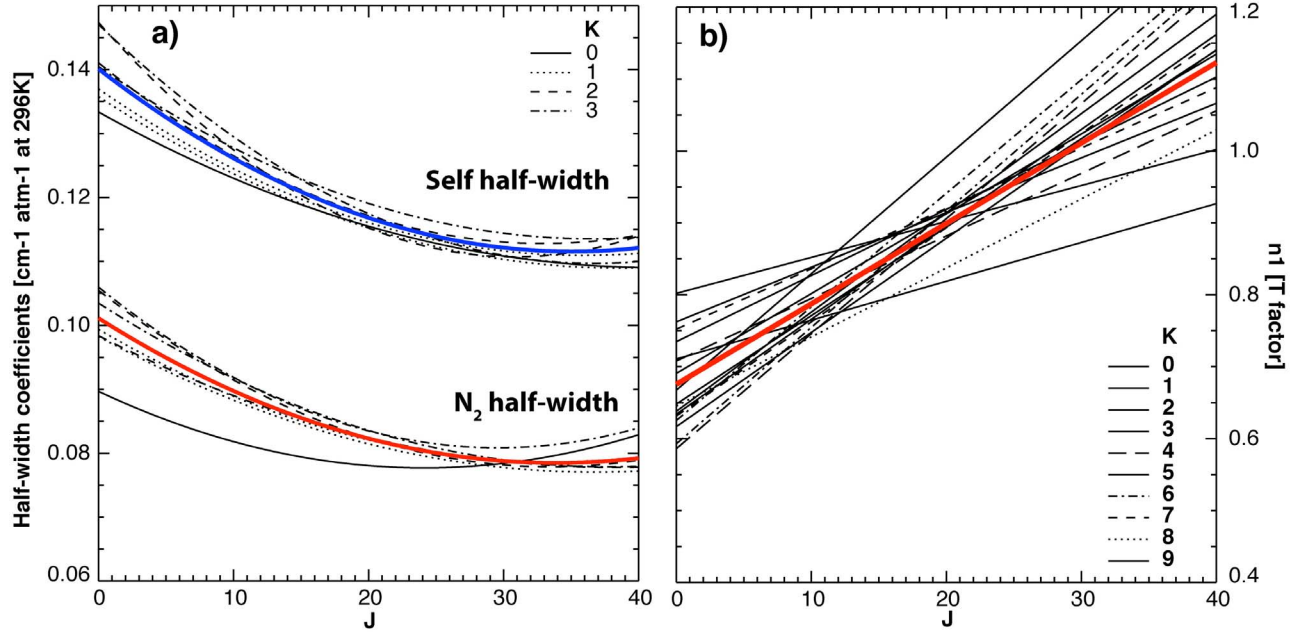


Figure 5. Lineshape parameters progressions retrieved by *Malathy Devi et al.* [2010a, 2010b] for ν_9 band of ethane and applied to our model of ν_7 band. For K values with no available measurements, we computed a weighted mean progression, shown by a thick color trace. Coefficients of weighted mean progressions are presented in Table 1f.

and ν_5), combination (e.g., $\nu_8 + \nu_{11}$), and hot bands (e.g., $\nu_7 + \nu_4 - \nu_4$) overlap at these wavelengths (Figures 3 and 6). *Harrison et al.* [2010] have gone to great extents to obtain accurate absorption cross sections for ethane at these wavelengths, with an overall uncertainty of 4%. Their cross sections were calibrated against PNNL spectra (Pacific Northwest National Laboratory IR database, <http://nwir.pnl.gov>), which are currently considered the gold standard for ethane. Considering these new absorption cross sections and taking into account the first torsional hot band (see section 2.6), we derived a S_ν^0 of $301\text{ cm}^{-2}\text{ atm}^{-1}$ for the ν_7 band, a correction of 14% with respect to the value previously reported by *Dang-Nhu et al.* [1984].

2.4. Einstein A_{21} Coefficients

[16] Einstein A coefficients were computed following *Šimečková et al.* [2006]:

$$A_{21} = \frac{8\pi c\nu^2 Q_{tot}(T)S_\nu(T)}{[1 - \exp(-hc\nu/kT)][\exp(-E''hc/kT)]I_a w'}, \quad (9)$$

where $Q_{tot}(T)$ is the total internal partition sum (TIPS) [*Fischer et al.*, 2003] (TIPS = 70,881 at 296 with $Q_\nu(296\text{ K}) =$

1.3732), and I_a is the isotopic abundance ($I_a = 0.97699$ for normal C₂H₆).

2.5. Lineshape Parameters

[17] *Malathy Devi et al.* [2010a, 2010b] reported an extensive and comprehensive study of line shape parameters (self- and N_2 -broadening half widths and their temperature dependence) for the ν_9 band (825 cm^{-1}) of ethane using a multispectrum analysis of data acquired at PNNL and the Jet Propulsion Laboratory. We applied the temperature dependence of the broadening coefficients using constants reported by *Malathy Devi et al.* [2010a, Table 2] for $K'' \leq 9$ and half-width coefficients (self and N_2) from *Malathy Devi et al.* [2010b, Table 5] for $K'' \leq 3$. For lines accessing K'' higher than the available measurements, we considered the mean progressions as presented in Figure 5. For pressure shifts, we consider the N_2 -broadened pressure-induced shifts of $-0.004\text{ cm}^{-1}/\text{atm}$ derived by *Pine and Stone* [1996] from RQ0 and PQ3 . A summary of the coefficients is presented in Table 1f.

2.6. Torsional Hot Bands

[18] Ethane has a low-energy torsional mode (ν_4) with its first excited level at 289 cm^{-1} ; thus, hot bands associated with

Table 1f. Spectroscopic Constants for ν_7 Band of Ethane: Line Shape Parameters for K Beyond Those Reported by *Malathy Devi et al.* [2010a, 2010b]^a

n_1 (N_2 Temperature Dependence)	n_2 (SELF Temperature Dependence)	$b_L^0(N_2)$ Width	$b_L^0(\text{SELF})$ Width
$A = 0.6756$ $B = 0.0112 (J_0 = 0)$	$A = 0.5687$ $B = 0.0085 (J_0 = 0)$	$a_0 = 0.1011$ $a_1 = -1.3352 \times 10^{-3}$ $a_2 = 1.9690 \times 10^{-5}$	$b_0 = 0.1401$ $b_1 = -1.6279 \times 10^{-3}$ $b_2 = 2.3211 \times 10^{-5}$

^aFor lines accessing K'' higher than those available by *Malathy Devi et al.* [2010a, 2010b], we considered the mean progressions as presented in Figure 5. The n_1 and n_2 coefficients are dimensionless, while the b_L^0 coefficients are in units of $\text{cm}^{-1}\text{ atm}^{-1}$ at 296K.

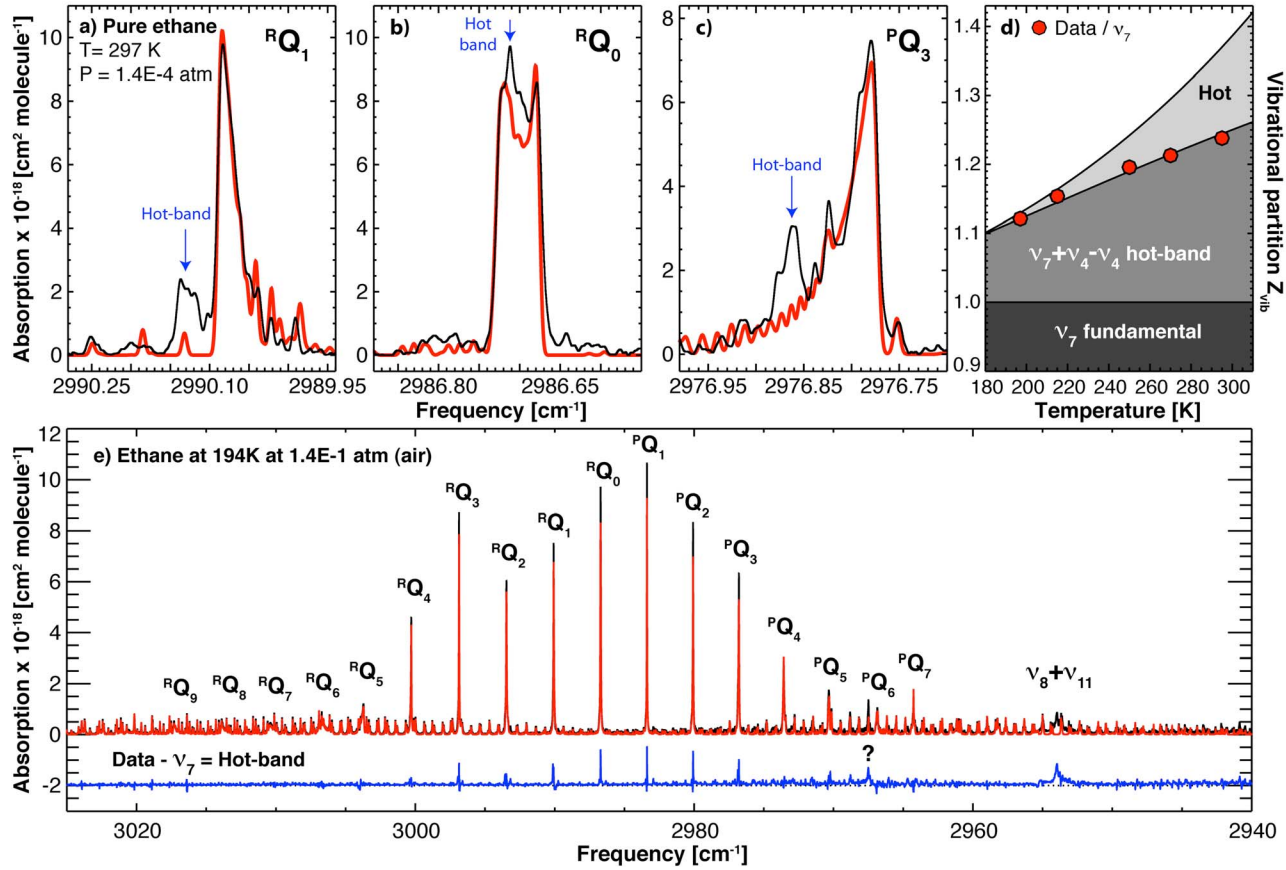


Figure 6. Identification of ν_7 hot band of ethane. (a–c) Comparisons of model spectra with pure ethane spectra recorded by Harrison et al. [2010] at 297 K and 1.4×10^{-4} atm. At these low pressures, the structure of the Q branches is nicely revealed, showing unaccounted absorptions that we associate with first torsional hot band of ν_7 band. (d) Ratio of area of strongest Q branches ($K'' \leq 4$, with the exception of PQ_1 ; see text) with respect to modeled ν_7 absorption, integrated around ($\pm 0.3 \text{ cm}^{-1}$) at each K band center. That ratio coincides with vibrational partition function of ν_7 level and its first torsional component suggests that these absorptions are related to $\nu_7 + \nu_4 - \nu_4$ hot band.

this level ($\nu_X + \nu_4 - \nu_4$) are relatively prominent at moderate temperatures. Spectroscopists have resorted to low temperatures and/or extremely high-resolution laboratory experiments to minimize/remove the confusion of hot and cold bands [e.g., Dang-Nhu et al., 1984; Pine and Stone, 1996]. Using sub-Doppler molecular-beam optothermal spectroscopy, Pine and Stone [1996] resolved the complex structure of the PQ_3 , RQ_0 , and RQ_3 subbands. Their measurements revealed new absorption lines, which Pine and Rinsland [1999] attributed to a torsional hot band ($\nu_7 + \nu_4 - \nu_4$, $E_g - A_{1u}$) with an intrinsic intensity ($S_{\nu,HOT}^0$) of $\sim 80\%$ to that of the fundamental (S_{ν}^0). Considering equation (6), the band intensity measured by Pine and Rinsland [1999] contributed $\sim 20\%$ ($80\% / 4$) of the ν_7 band at 296 K considering that the summed population in the first torsional level is one fourth as large as that of the ground state at 296 K. The hot band contribution is greatly reduced at cometary temperatures and, for instance, at 100 K is only 1% if we assume that vibrational populations are thermally equilibrated.

[19] Unfortunately, there are no spectral constants for the $\nu_7 + \nu_4 - \nu_4$ band, and Pine and Rinsland [1999, Table 1] only

provided coarse estimates for parameters of the hot analog of the PQ_3 subband by simulating the band contour observed by Pine and Stone [1996]. The $\nu_7 + \nu_4 - \text{ground}$ ($E_g - A_{1g}$) combination band is observable through Raman spectroscopy and was tentatively detected by Fernández and Montero [2003], although the low signal-to-noise ratio limited the extraction of reliable rotational constants for the $\nu_7 + \nu_4$ vibrational level. However, their measurements predict the location of the hot band to be in the 2984–2950 cm^{-1} frequency range, consistent with the findings of Pine and Rinsland [1999] and with our results (Figure 6).

[20] We see strong extra absorption near the Q branches of the ν_7 band (Figures 6a–6c). We investigated the temperature dependence of these features by integrating around ($\pm 0.3 \text{ cm}^{-1}$) the strongest Q branches, and observed that the ratio of data and model (Figure 6d) coincided with the vibrational partition function of the ν_7 level and its first torsional component, confirming the origin of this absorption to be the $\nu_7 + \nu_4 - \nu_4$ hot band. We excluded the PQ_1 branch from the analysis because it appeared slightly saturated in the Harrison et al. [2010] data set. Due to the strong spectral

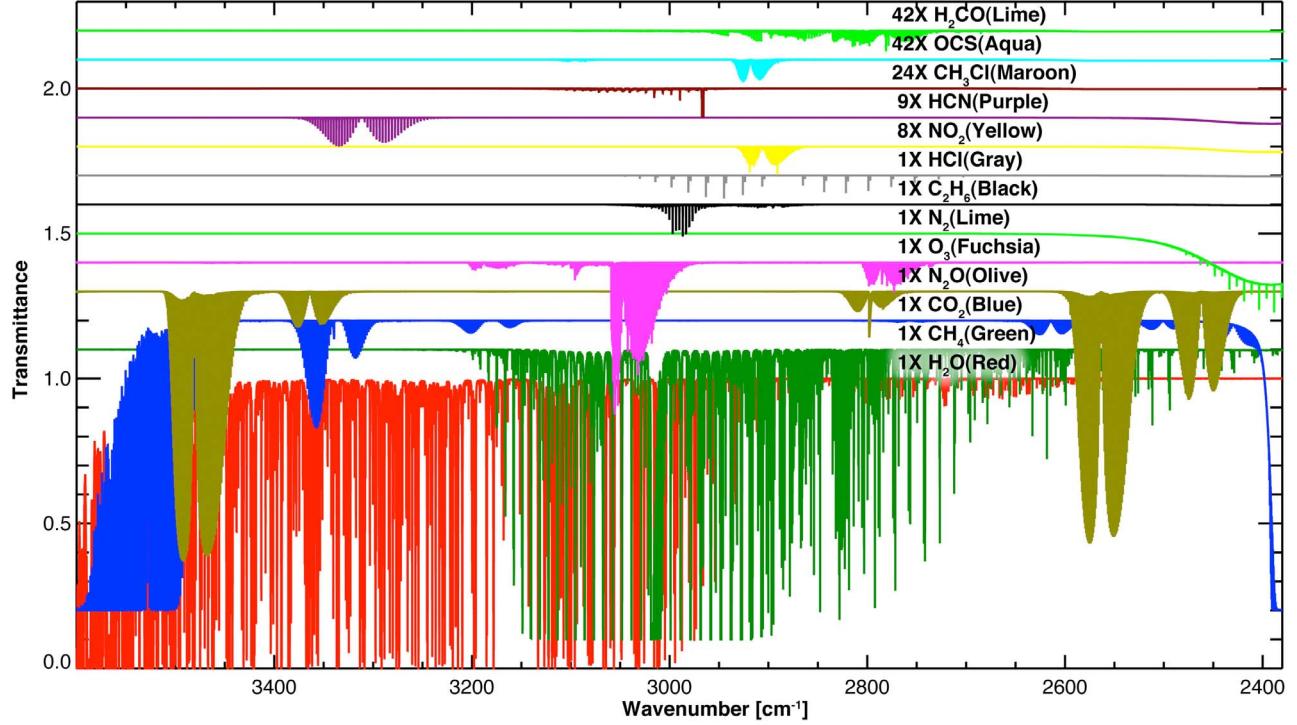


Figure 7. Representative terrestrial spectra synthesized with LBLRTM (line-by-line and layer-by-layer radiative transfer model), using our updated spectral database. Spectra were synthesized at air mass of 1.0 (zenith), and adopting nominal abundances, temperatures, and pressures for Mauna Kea at 4200 m altitude.

confusion and complexity of this hot band system, it is not yet possible to extract reliable constants for this hot band system.

[21] At 296 K, the observed intensity of the hot band was 25% with respect to the fundamental ($\Sigma S\nu_{7HOT}(296 \text{ K}) / \Sigma S\nu_7(296 \text{ K})$), similar to the findings of Pine and Rinsland [1999] for the PQ_3 replica of ~20%. Perhaps a technique as considered by Oomens and Reuss [1996] to study the $\nu_7 + \nu_9 - \nu_9$ hot band of ethane should be employed to fully characterize the $\nu_7 + \nu_4 - \nu_4$ hot band. We currently account for the existence of the hot band in our moderate-resolution spectra by computing a simplistic $\nu_7 + \nu_4 - \nu_4$ line list that considers the rotational constants of ν_4 from Blass *et al.* [1990] (neglecting torsional subspecies), and fitted constants for the $\nu_7 + \nu_4$ using the data presented in Figure 6.

2.7. Machine-Readable Spectral Atlas

[22] Following the preceding guidelines, we computed 17,266 spectral lines with $K_{\max} = 20$ and $J_{\max} = 40$ in the 2900–3100 cm^{-1} frequency range; 8680 for the ν_7 band and 8586 for the hot band. The database has been organized following the HITRAN 2008 format with line identifications following the G^+_{36} point group model. To allow for future investigations of conversion efficiencies between different symmetries, we report lines for each symmetry individually, even if the lines are not resolved (e.g., a $A_{34s}-A_{12s}$ line is reported as two lines: $A_{3s}-A_{1s}$ and $A_{4s}-A_{2s}$). The vibrational indicators are V7, GROUND, V7 + V4 and V4, whereas the local quantum numbers are J , K , and ℓ . The atlas for the ν_7 band has been provided to the HITRAN team for further integration into their consolidated database. Due to the large

uncertainty in the rotational constants of the hot band, we only provide the atlas of the hot band on request for use with moderate resolution spectra only.

3. Modeling of Ethane in Terrestrial Atmospheres (LTE Case)

[23] Ground-based spectra of extraterrestrial and cometary atmospheres are affected by telluric absorption. The incoming spectral lines are often Doppler broadened, and they experience extinction by atmospheric lines that approach the Doppler-broadened limit (e.g., gases with significant stratospheric and mesospheric components, such as CH_4 , CO_2 , and O_3). Analysis of spectra measured for such lines requires that telluric transmittance be synthesized at sub-Doppler resolution (a spectral resolution of not more than 100 m/s, or 0.001 cm^{-1} at 3000 cm^{-1}). We applied the new model for C_2H_6 (ν_7 and torsional hot band) to synthesize terrestrial spectra using an advanced radiative transfer code for the terrestrial atmosphere that accesses a customized database of spectral constants from 42 molecules including C_2H_6 (Figure 7 and Appendix A).

[24] Proper synthesis of terrestrial spectra requires line-by-line, layer-by-layer radiative transfer modeling of the atmosphere, in which the quality of the synthesized spectrum depends directly on the robustness of the used set of radiative transfer equations, the precision of the adopted spectroscopic constants, and the accuracy of the assumed atmospheric conditions (Figure 8; $P(z)$, $T(z)$, abundance profiles, and geometric conditions). Until 2005, we used the spectrum synthesis program (SSP) [Kunde and Maguire, 1974] accessing

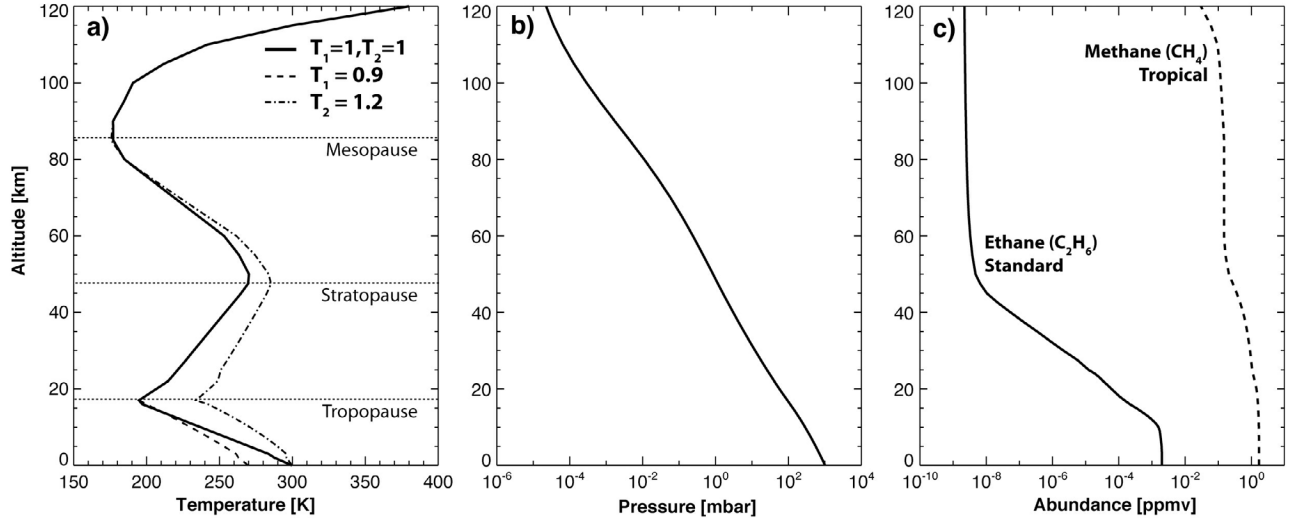


Figure 8. Vertical profiles of (a) temperature, (b) pressure, and (c) mixing ratios for CH_4 and C_2H_6 adopted for synthesizing terrestrial spectra. The temperature profile is organized into tropospheric (affected by T_1) and stratospheric (affected by T_2) sectors (Figure 8a); pressure profile is standard tropical pressure profile scaled with a multiplier (Figure 8b). Temperatures and pressures are scaled relative to standard tropical value [Anderson *et al.*, 1986].

the HITRAN 1992 [Rothman *et al.*, 1992] to compute terrestrial spectra. From 2005 until 2009, we used the more advanced GENLN2 v4 model [Edwards, 1992], which provides highly realistic and Doppler-limited spectral synthesis of the terrestrial atmosphere. We improved the GENLN2 v4 model by providing a correction to properly account for spectral pressure shifts and introducing the capability to access the latest HITRAN databases [Villanueva *et al.*, 2008a]. However, GENLN2 is no longer supported by National Center for Atmospheric Research, Boulder, Colorado.

[25] In 2005, a new efficient line-by-line radiative transfer became available, the LBLRTM [Clough *et al.*, 2005]. Perhaps, one the biggest advantages of this code relative to GENLN2 is that it is highly optimized, allowing us to increase the number of layers and the number of spectral points for the same computation time, ultimately achieving a more realistic atmospheric solution. In addition, this code is maintained by Atmospheric and Environmental Research, Inc. (AER) and has been (and continues to be) extensively validated against atmospheric spectra from the ultraviolet to the submillimeter. Even though the AER team provides a compiled spectral database to use with its LBLRTM, we have preferred to instead use the more universally recognized HITRAN atlas as the base for our radiative transfer modeling (using LBLRTM) with our own corrections and updates tailored to our requirements (Appendix A).

[26] Using our updated spectral database and LBLRTM, we synthesized spectra for the complete *L* band (2.8–4.2 μm ; Figure 7), with a spectral resolution of 0.0005 cm^{-1} and consistent with a mean sampling power of \sim 5 million ($\lambda/\Delta\lambda$), or a velocity resolution of 60 m s^{-1} . This novel method has been successfully applied to calibrate and process infrared spectra of planets (Figures 9 and 10) and comets (Figures 12–

14) taken with several instrument/telescope combinations (section 5).

[27] Even though we obtain very good results with our ethane ν_7 band model, the line list is based on a restricted set of spectral constants, and this ultimately leads to limited precision and accuracy. These imprecisions could cause assignment of improper transmittance values for some incoming ethane lines due to accidental overlap with Doppler-broadened lines of stratospheric O_3 . Further empirical studies are needed to properly characterize the complete structure of this band, including a full description of torsional tunneling splittings, overtone perturbations, hot bands, and A_1 - A_2 doublings for all *K* subbands. We intend to expand our model as more complete ethane line parameters are obtained.

4. Modeling of Ethane in Cometary Atmospheres (Nonlocal Thermodynamic Equilibrium Case)

[28] The C_2H_6 ν_7 band is particularly bright in hydrocarbon-rich comets where efficient solar pumping (and inefficient collisional quenching) leads to strong C_2H_6 fluorescence emission. The complexity of the band in comets is revealed in Figures 12–14. The torsional mode is inactive to radiative decay, and little is known about its possible collisional quenching or excitation. It is possible that the vibrational partitioning (of ν_4) imparted on release at the cometary nucleus is maintained throughout the inner coma, and thus the torsional manifold could become increasingly disequilibrated from the rotational and kinetic distributions as the gas flows outward through the coma, ultimately permitting pumping from the torsional level and leading to ν_7 hot-band fluorescent emission. Our cometary data show no evidence of strong hot-band emission, but higher spectral resolution and a better understanding of the spectral character

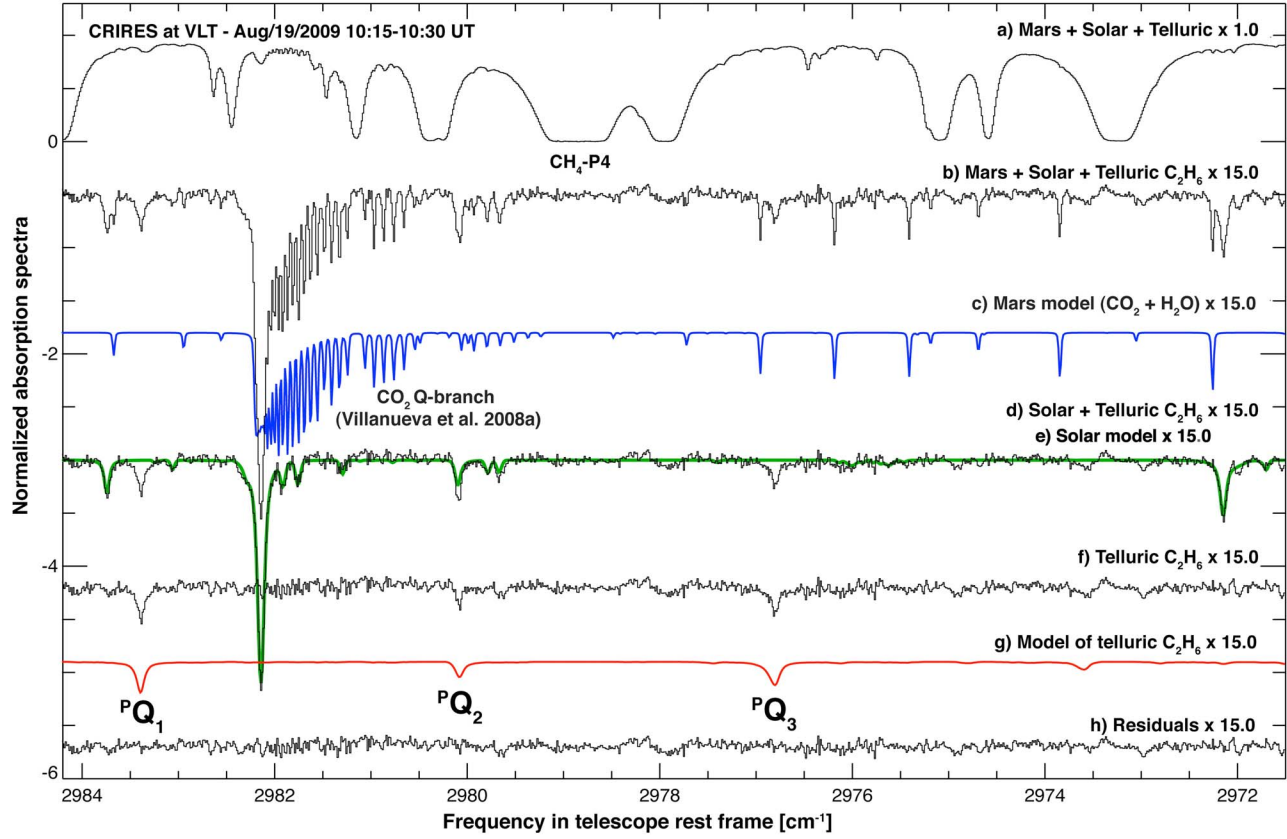


Figure 9. Mars infrared spectrum taken on 18 August 2009 with CRIRES at VLT (total of 8 minutes of integration time on source). (a) Calibrated Mars continuum affected by terrestrial transmittance, and (b) Mars residual spectrum after removing a terrestrial model (with no C_2H_6). (d) Residual spectrum after removing (c) a Martian absorption spectrum containing CO_2 and H_2O . (d) Residual spectrum containing solar Fraunhofer lines and telluric C_2H_6 lines, and (e) model of solar spectrum considering new method presented in Appendix B. (f) Residual telluric ethane spectrum and (h) overall residual after removing (g) a terrestrial spectrum synthesized with our new C_2H_6 ν_7 band model.

of the hot band is necessary to test its contribution or lack thereof to the total flux in the ν_7 region.

[29] Collision partners in cometary atmospheres usually lack sufficient energy to excite vibrational transitions and the rate of quenching collisions is much smaller than radiative decay rates for (infrared-active) excited states. Thus, the vibrational manifold is not populated in local thermodynamic equilibrium (LTE). Instead, solar radiation pumps the molecules into an excited vibrational state, which then deexcites by rapid radiative decay. Infrared photons are emitted through decay to the ground vibrational state, either directly (resonant fluorescence) or through branching into intermediate vibrational levels (nonresonant fluorescence). Resonance fluorescence is the expected dominant factor in the excitation and the sole pumping mechanism we consider here, although additional excitation cascading from levels with energies higher than ν_7 may also be active. We expect to expand the excitation for nonresonant fluorescence of the model, once spectroscopic data of related bands become available.

[30] Since fluorescence is a non-LTE process, computation of line-by-line fluorescence efficiencies (g factors) entails the building of a full quantum mechanical model. This requires precise knowledge of the rotational structure (energy levels)

for each vibrational level involved, statistical weights, selection rules, perturbations (e.g., Coriolis effects, splittings, tunneling), and band emission rates. The difficulty of this task has limited the development of new models, particularly for those molecules having a complex symmetry structure, and, consequently, only a limited set of line-by-line fluorescence emission models are currently available. In the case of C_2H_6 , previous attempts to model ν_7 fluorescence in comets focused only on integrated Q branch intensities but did not specify the fine rotational structure, aside from adopting a specific rotational temperature [Mumma et al., 1996; Dello Russo et al., 2001].

[31] Another problem with most current cometary (infrared) fluorescence models is that they often assume that the source for solar pumping is a simple blackbody continuum with an effective temperature of the Sun. This approximation is somewhat correct for the continuum flux at certain wavelengths ($2900\text{--}3300\text{ cm}^{-1}$), but it leads to inaccuracies when computing pumping rates for individual rovibrational lines if the relative heliocentric velocity of the comet shifts the pumping radiation field into solar absorptions (Swings effect). Omitting this effect will introduce not only a relative error, but it will also lead to incorrect retrievals of rotational

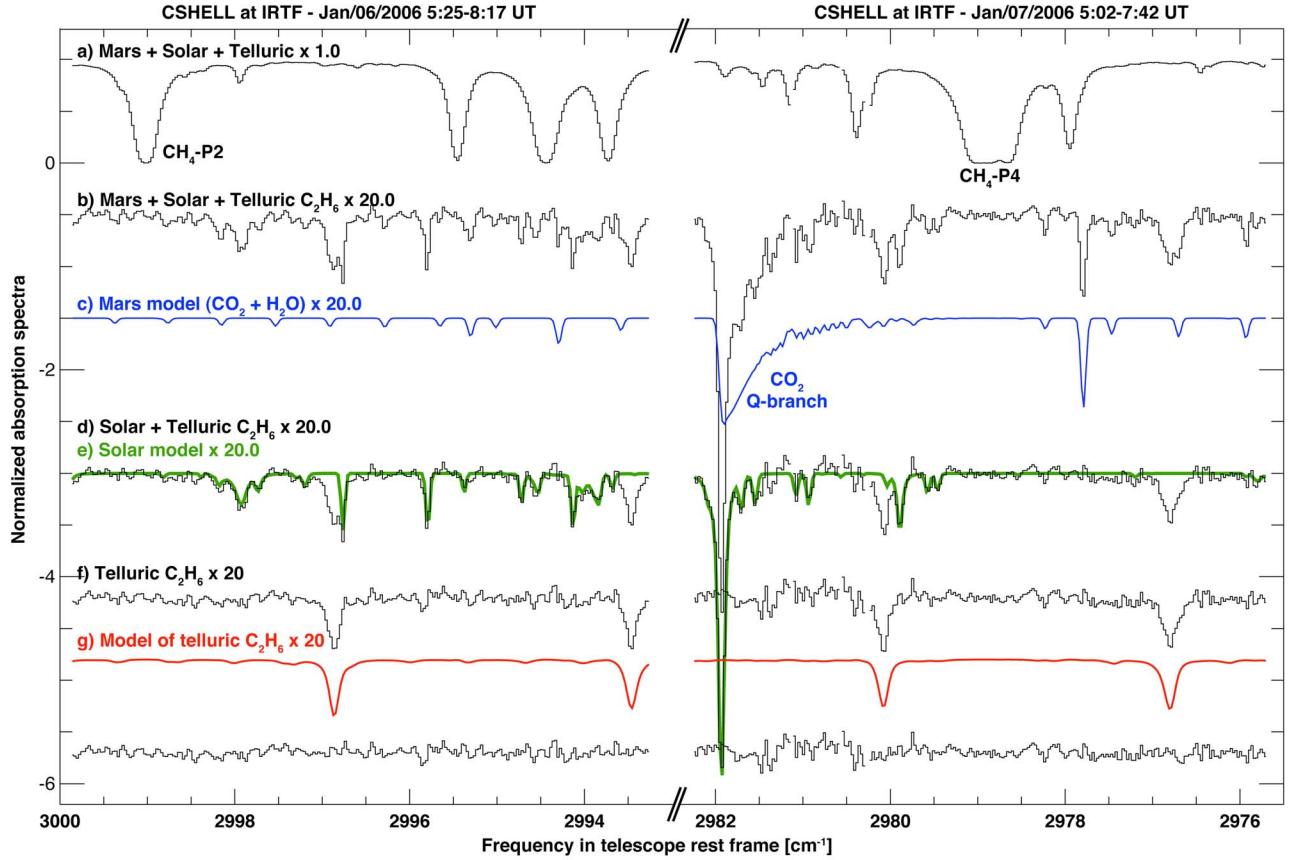


Figure 10. Mars infrared spectra taken on 6–7 January 2006 using two CSHELL-IRTF settings (total integration time on source was 40 (52) minutes for left (right) spectrum). See Figure 4 for description of traces. Spectral sharpness of spectral features is higher in Figure 8 because of higher resolving power ($\lambda/\Delta\lambda \sim 90,000$) with CRIRES (for CSHELL, $\lambda/\Delta\lambda \sim 40,000$). Terrestrial C₂H₆ lines appear stronger in Northern Hemisphere (compare to Southern Hemisphere spectra, Figure 9) because of higher abundance of volatile organic compounds (including C₂H₆) that arise mainly from biogenic and anthropogenic emissions.

and spin temperatures since these are derived from line-to-line intensity ratios. We replace the adopted blackbody radiation field with a synthesis of the true solar spectra using a combination of empirical parameters from the solar spectrum [Hase *et al.*, 2006, 2010] calibrated with a stellar continuum flux model (see combined Web/outgoing-FTP site, <http://kurucz.harvard.edu/>); see Appendix B for a full discussion.

[32] Fluorescence emission rates (*g* factors) are normally quantified as energy (or quanta) emitted per second per molecule in units of (J s⁻¹ mol⁻¹), (W mol⁻¹), (photon s⁻¹ mol⁻¹), or simply (s⁻¹), and are computed following a two-step process: (1) pumping to the excited state and (2) relaxation to lower levels. The spectral constants needed to compute *g* factors can be extracted from an atlas of molecular lines, like HITRAN, if the tabulated data are adequate. When validated, these databases are extremely valuable repositories of the latest spectral constants and line parameters that can be influenced by complex perturbations such as Coriolis effects, splittings, resonances, and tunneling. Consequently, we developed a general fluorescence model to compute fluorescence emission rates (Appendix C) and applied it to our ethane line lists (hot and cold ν_7 bands) by creating a complete atlas for this band system (as reported in section 2).

Apart from C₂H₆ ν_7 (this work) and ν_5 [Radeva *et al.*, 2011], we successfully applied this approach to other infrared band systems (ν_1 of HCN, ν_3 of CH₄, 1–0 bands of CO and ¹³CO, ν_1 and $2\nu_2$ of HDO, ν_3 and $\nu_2 + \nu_4 + \nu_5$ of C₂H₂) (G. L. Villanueva *et al.*, manuscript in preparation, 2011).

5. Discussion of Models and Fluorescence Efficiency

5.1. Local Thermodynamic Equilibrium Validation: Results From Ground-Based Measurements

[33] We validated our synthetic terrestrial models by comparing them to infrared spectra of Mars and comets acquired with different spectrometer/telescope combinations: CRIRES [Käufl *et al.*, 2004] at the Very Large Telescope (VLT) in Chile, Cryogenic Echelle Spectrometer (CSHELL) [Tokunaga *et al.*, 1990] at the NASA-InfraRed Telescope Facility (IRTF) in Hawaii, and NIRSPEC [McLean *et al.*, 1998] at the Keck II telescope in Hawaii.

[34] In August 2009, we observed Mars using the CRIRES instrument, sampling the planet at its midafternoon along meridian longitudes passing through Syrtis Major (an ancient shield volcano) and the Hellas impact basin (geometry shown

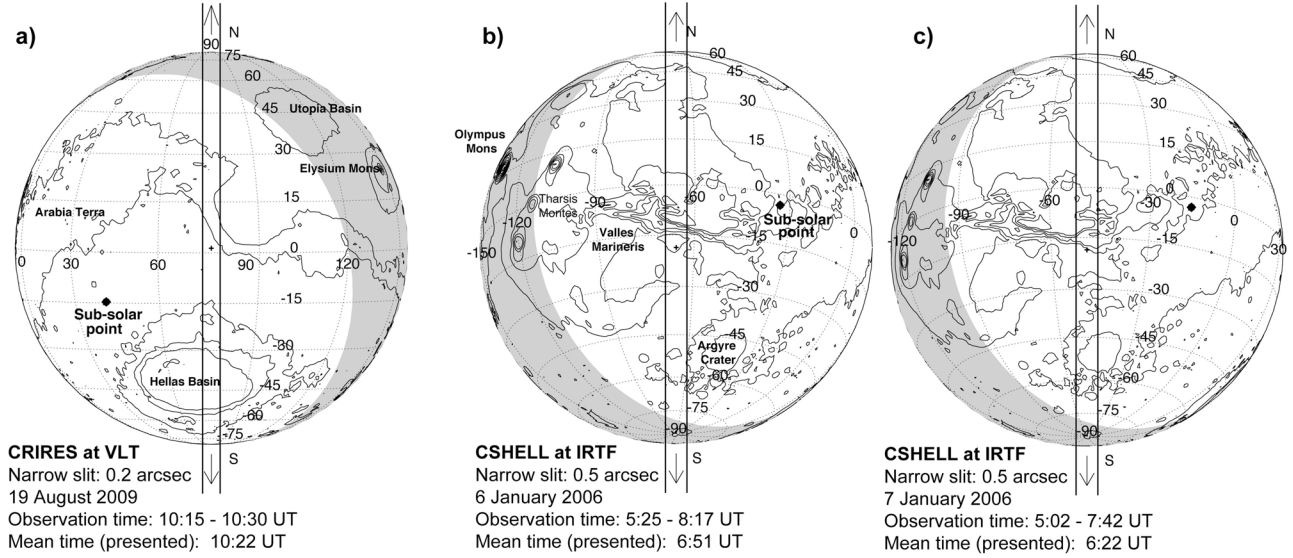


Figure 11. Geometry diagrams presenting the orientation of the spectrometer's entrance slit for (a) CRIRES data taken on 19 August 2009 and (b and c) CSHELL data taken on 6–7 January 2006. The narrowest slit was used for each instrument (0.2" for CRIRES, 0.5" for CSHELL), and oriented slit North-South on the planet for three measurements.

in Figure 11a). These observations reveal the recently discovered CO₂ band (Mars), multiple lines of water (Mars, Earth), and the telluric absorption spectrum of the ν_7 band of C₂H₆ (Figure 9). In January 2006, we sampled Mars at its midmorning along meridian longitudes passing through Valles Marineris and the Argyre impact basin (geometry shown in Figures 11b and 11c), using two CSHELL settings obtained on 2 consecutive days (Figure 10).

[35] For each observatory, we synthesized terrestrial transmittance and radiance spectra for C₂H₆ and other species by assuming default geometric conditions for that high-altitude site, assuming clear atmospheric conditions (no aerosols), 50 (optically thin) atmospheric layers, and LTE populations. The atmospheric conditions (pressure, temperature, and abundances) are based on a standard tropical profile (Figure 8), modified to describe the observing conditions through two temperature parameters (T_1 and T_2), a pressure scaling factor (PF) and abundance factors (AF ; see profiles for CH₄ and C₂H₆ in Figure 8c). The given pressure profile is scaled following $P'(z) = P(z) \times PF$, whereas the temperature profile is divided into tropospheric (affected by T_1) and stratospheric (affected by T_2) (Figure 8a) sectors. The abundance profiles are scaled relative to the tropical profile by a molecular multiplier relative to the tropical value. For each data set, we retrieved abundances and the atmospheric parameters (T_1 , T_2 , PF) using a Levenberg-Marquardt nonlinear-minimization algorithm that compares the transmittance model to the absorption features observed against the planetary continua.

[36] Agreement of the terrestrial ethane residuals and synthesized spectra is very good, revealing strikingly different C₂H₆ abundances at Mauna Kea in Hawaii and Cerro Paranal in northern Chile. In particular, the CH₄ abundance was nominal for both sites, but the C₂H₆ abundance showed important seasonal variations and extremely low values for the Southern Hemisphere. At first, we were concerned that

inaccuracies of the ν_7 band model introduced these excursions; however, prior independent investigations confirm our retrievals [e.g., Rinsland et al., 2002; Glatthor et al., 2009]. For instance, the recent study of Helmig et al. [2009] reports similar trends from a vast global monitoring program of volatile organic compounds, including C₂H₆. Both CH₄ and C₂H₆ mostly arise from biogenic and anthropogenic emissions, although methane has a much longer lifetime (~8 years) than ethane (months) [see Hough, 1991] in the terrestrial atmosphere.

[37] The short ethane lifetime causes important fluctuations in its atmospheric concentration since the sources and sinks vary geographically and seasonally. This is particularly evident in the Southern Hemisphere where anthropogenic emissions are much smaller, leading to a C₂H₆ maximum seven times lower than in the Northern Hemisphere [Helmig et al., 2009], consistent with our findings (Table 4). At the summit of Mauna Kea, we observe an equivalent volume mixing ratio (VMR) of 1 ppb, similar to that of Rinsland et al. [1994] (1.1 ppb) for Mauna Loa at this season. The retrievals from Rinsland et al. [1994] were based on the ν_7 PQ_3 subbranch of ethane, but they ignored the presence of the hot-band absorption from the $\nu_7 + \nu_4 - \nu_4$ band [Pine and Rinsland, 1999] at these frequencies. If we attempt to revise the values from Rinsland et al. [1994] considering hot-band absorption and the new band intensity from PNNL spectra, then their VMR would become ~1 ppb, in excellent agreement with our results. These consistencies, together with the excellent agreement we obtained when we compared the synthetic models to spectra taken using different instruments (Figures 9, 10, and 12–14), are important validations of the ν_7 line-by-line model (including our updated spectral database) and the radiative transfer modeling.

[38] By properly accounting for the telluric absorption of C₂H₆ in this spectral region, we obtain better quality residuals, ultimately allowing us to perform very sensitive

Table 2. Symmetries of Rotational Levels of Ground and ν_7 Vibrational States Considering D_{3d} and G^+_{36} Point Groups^a

Level	ℓ	K	J	D_{3d} Notation	G^+_{36} Notation
Ground (A_{1g})	0	0 1,2,4,5 3,6,9	0,2,4	$A_{1g}(8)$	$A_{1s}(6) + E_{3s}(2)$
			1,3,5	$A_{2g}(16)$	$A_{2s}(10) + E_{4s}(6)$
			All	$E_g(20)$	$E_{1s}(4) + G_s(16)$
ν_7 (E_u)	-1	0,1,3,4,6,7		$A_{1g}(8) + A_{2g}(16)$	$A_{1s}(6) + E_{3s}(2) + A_{2s}(10) + E_{4s}(6)$
		2,5,8		$E_u(20)$	$E_{2s}(4) + G_s(16)$
	+1	0,2,3,5,6,8 1,4,7		$A_{1u}(8) + A_{2u}(16)$	$A_{3s}(6) + E_{3s}(2) + A_{4s}(10) + E_{4s}(6)$
				$E_u(20)$	$E_{2s}(4) + G_s(16)$
				$A_{1u}(8) + A_{2u}(16)$	$A_{3s}(6) + E_{3s}(2) + A_{4s}(10) + E_{4s}(6)$

^aThe G^+_{36} permutation-inversion group is used when internal torsional tunneling is considered. Statistical weights for each spin species are presented in brackets.

searches for biomarker gases on Mars and other astronomical objects. Using the residuals presented in Figures 9 and 10, we obtained the most sensitive upper limits for ethane on Mars ever measured (Table 4). We can expect immediate improvement in these upper limits by including additional spectral scans.

5.2. Solar Spectrum: Extraterrestrial and Cometary Spectra

[39] The precise modeling of the solar spectrum is particularly important when observing planetary bodies in reflected light (e.g., Mars, Moon). The infrared radiation observed from Mars is a combination of reflected sunlight (with Fraunhofer lines) and planetary thermal emission (featureless continuum). Sparse spectral lines of Mars' atmospheric constituents are superposed on the continua according to the

optical path experienced by the two components (Figures 9 and 10). Sunlight experiences a double optical path (Sun-to-surface + surface-to-observer), whereas the Mars "thermal" continuum traverses only a single path (surface-to-observer). We determine the relative contributions of solar and thermal emission to the measured continuum by comparing the measured area (equivalent width) of Fraunhofer lines with their true value (Appendix A). This permits identification of the "effective" optical path needed to properly determine molecular abundances on Mars [see Villanueva et al., 2008a; Novak et al., 2002], and thus an accurate solar model has impact not only on the spectral residuals but also on the retrieval process.

[40] The signal-to-noise ratio (SNR) of the adopted solar spectrum limits the maximum achievable quality of the residuals. At 3 μm , the typical SNR of the ATMOS solar

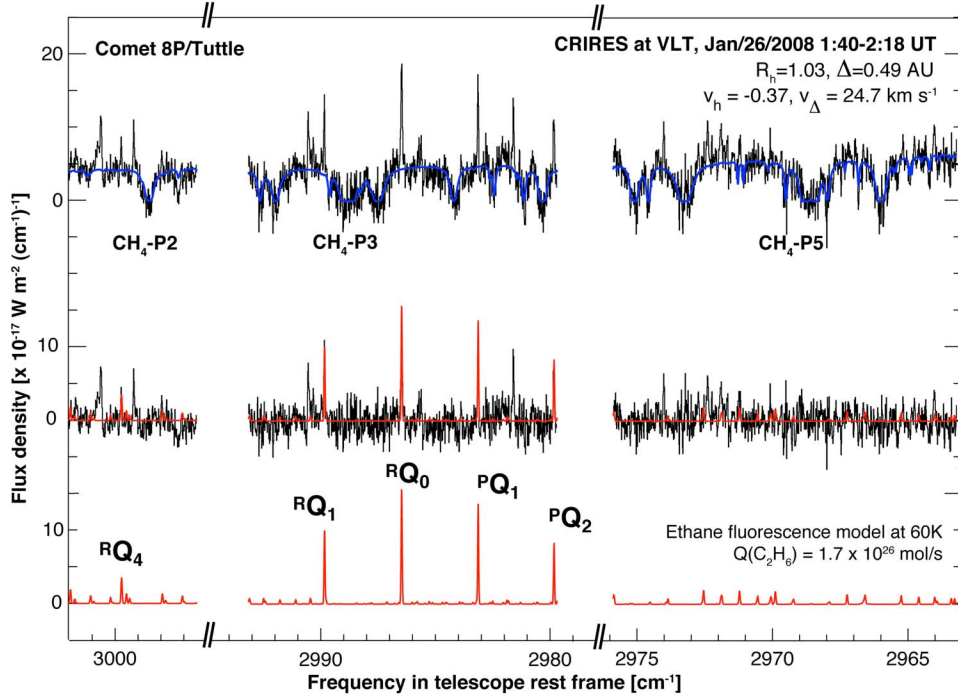


Figure 12. Infrared spectrum of comet 8P/Tuttle taken on 26 January 2008, using CRIRES at VLT [Böhnhardt et al., 2008]. The upper trace shows a spectrum extracted from the sum of 15 spatial rows centered on comet nucleus, and a continuum model affected by terrestrial transmittance is overlaid. The midtrace residual spectrum on the comet nucleus reveals lines of the ν_7 band of C_2H_6 in emission (with model overlaid).

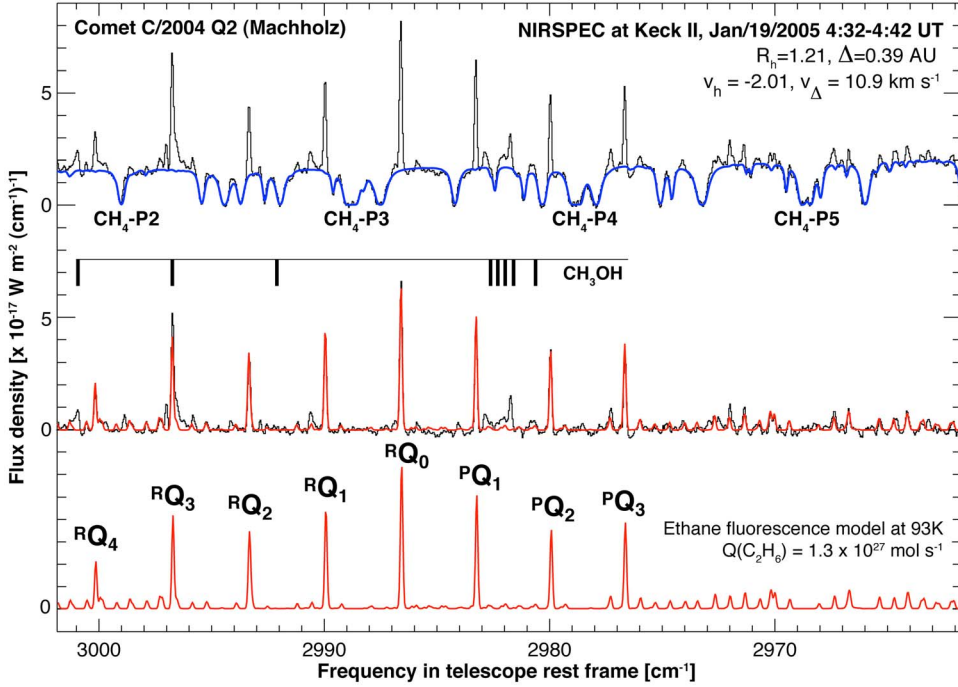


Figure 13. Infrared spectrum of comet C/2004 Q2 (Machholz) taken on 19 January 2005, using NIRSPEC at Keck II [Bonev et al., 2009]. The upper trace shows a measured spectrum extract from the sum of nine spatial rows centered on the comet nucleus, and a continuum model affected by terrestrial transmittance is overlaid. The midtrace shows residual emission revealing lines of the ν_7 band of C_2H_6 (with model overlaid) and certain CH_3OH lines.

spectrum [Abrams et al., 1996] is ~ 1000 (1σ), a sensitivity achievable in minutes with most bright infrared sources (e.g., Mars, flux standard stars) using current high-resolution spectrometers.

[41] To increase the SNR of the residuals, we combined empirical and observational data from ground- and space-based instruments to obtain an improved model for the solar spectrum (Appendix B). This new solar spectrum will greatly contribute to the search for weak spectral signatures within solar reflected sunlight; this is demonstrated in Figures 9 and 10, where we observe excellent agreement between the solar features imprinted in the Mars continua and those synthesized with the new solar model.

[42] The precise description of solar features is of paramount importance when studying solar pumped fluorescence in comets. The use of a nonrealistic solar pumping flux would introduce, for example, errors up to 30% for certain g factors of the ν_7 band of C_2H_6 and up to 40% for selected lines of the 1–0 band of CO. Because this (Swings) effect depends on the heliocentric velocity of the comet, fluorescence rates need be computed for each orbital situation using the synthesized solar spectrum described in equation (C.3).

5.3. Validation of Fluorescence Efficiency Factors: Comets

[43] We have chosen three cometary data sets (8P/Tuttle, C/2007 W1 (Boattini), C/2004 Q2 (Machholz)) to test the new C_2H_6 fluorescence model. These comets displayed bright ethane emissions and different rotational temperatures, in spectra acquired with CRIRES and NIRSPEC. Comet

8P/Tuttle (hereafter 8P) was observed in January–February 2008 using CRIRES at the VLT with the adaptive optics (AO) system (Figure 12). Using AO minimizes slit losses and achieves an increased SNR in the central part of the coma. The spatial resolution along the slit is high as well and is close to the diffraction limit of the telescope.

[44] Results for six volatiles including C_2H_6 were presented by Böhnhardt et al. [2008]. At the time of observations (26 January 2008), the cometary ephemerides were $r_h = 1.03$ AU (heliocentric distance), $\nu_h = -0.37$ km s^{-1} (heliocentric velocity of the comet), $\Delta = 0.49$ AU (geocentric distance), and $\nu = 24.7$ km s^{-1} (geocentric velocity of the comet), and (as retrieved from 19 water lines) the nucleus-centered rotational temperature was 60^{+8}_{-9} K for H_2O . We synthesized a fluorescence model for C_2H_6 for the previously mentioned conditions, and retrieved a C_2H_6 production rate of $(1.74 \pm 0.06) \times 10^{26}$ mol s^{-1} for 8P, an improvement in the confidence limits of a factor of 3 (Figure 15), with respect to the previously reported value derived with the old ethane fluorescence model (compare 8P values in Table 4 and in work given by Böhnhardt et al. [2008]).

[45] A similar improvement was obtained with spectra of comet C/2004 Q2 (Machholz) (hereafter Q2), which was observed using NIRSPEC in November 2004 and January 2005 [Bonev et al., 2009]. We applied the new C_2H_6 model to the spectra taken on 19 January 2005 (Figure 13) and retrieved a production rate of $(13.3 \pm 0.25) \times 10^{26}$ mol s^{-1} at 93 K (a correction of -12% to the value reported previously), with a confidence limit improved by a factor of 3. Considering a $Q(\text{H}_2\text{O})$ of $(2.727 \pm 0.070) \times 10^{29}$ mol s^{-1} as reported

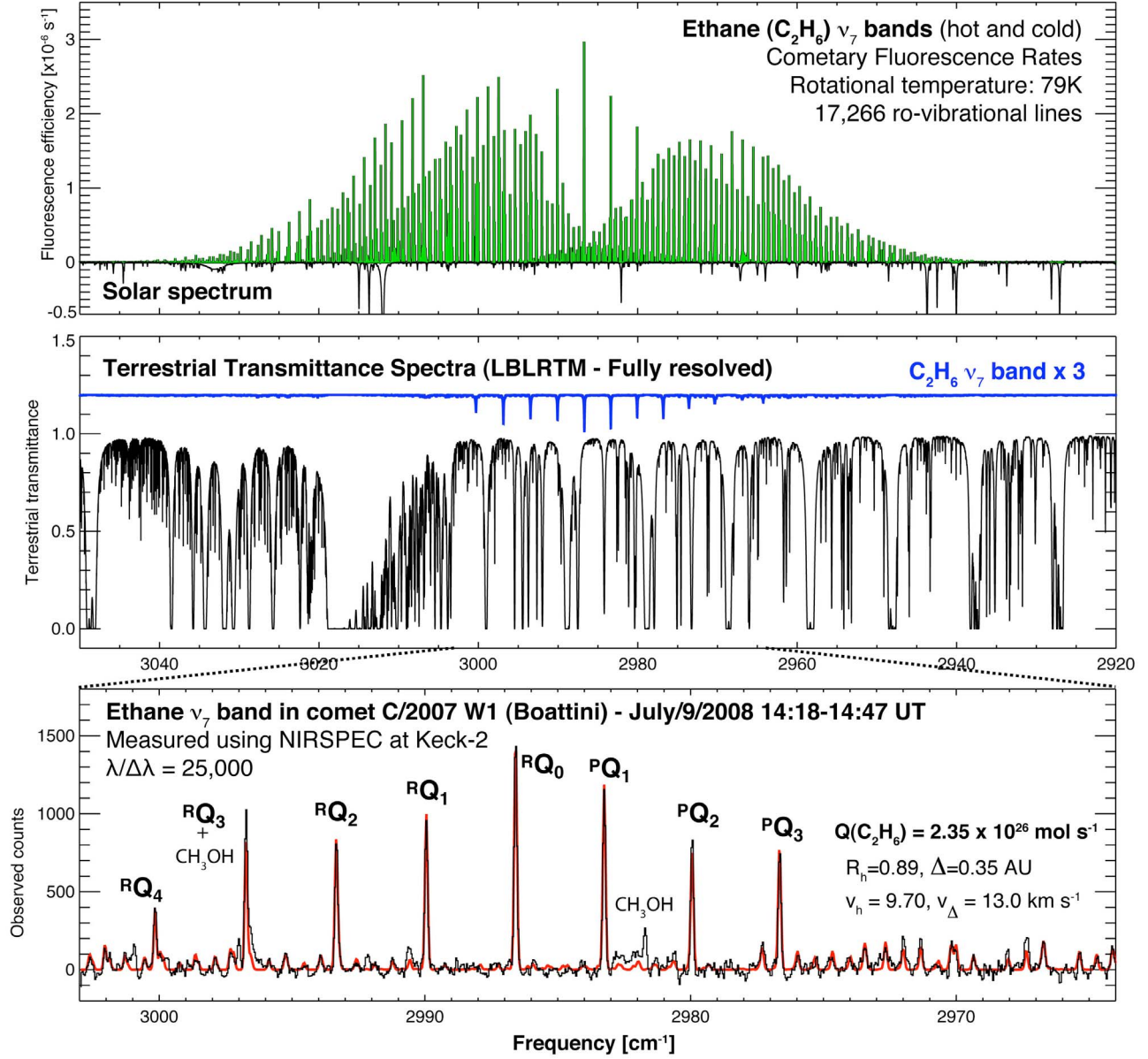


Figure 14. Fluorescence model of the ν_7 bands of C_2H_6 and comparison with spectra of comet C/2007 W1 (Boattini) taken on 10 July 2008 with NIRSPEC at Keck II. (top) Ethane fluorescence emission rates (g factors) for 17,266 lines of ν_7 (fundamental band) and $\nu_7 + \nu_4 - \nu_4$ (hot band) with $T_{rot} = 79 K$, $v_h = +9.70 km s^{-1}$, and $R_h = 1AU$. (middle) Terrestrial transmittance and telluric C_2H_6 absorption synthesized using LBLRTM. (bottom) High-resolution spectrum of comet Boattini showing the fine structure of the ν_7 band of C_2H_6 (with model overlaid) and certain CH_3OH lines.

by Bonev et al. [2009] for this date, this would correspond to an ethane mixing ratio of $0.488 \pm 0.016\%$. This mixing ratio is consistent with that derived from the ν_5 band of ethane for 28 November 2004 by Radeva et al. [2011] of $0.48 \pm 0.06\%$. Last, comet C/2007 W1 (Boattini) (hereafter W1) was observed in July 2008 using NIRSPEC (Figure 14). The comet has a particularly rich chemistry, and the ethane Q branches are very bright in our spectra. From the comaeasured water spectrum and considering 20 lines of H_2O , we retrieved a rotational temperature of $79 \pm 3 K$ for H_2O on 9 July 2008 (G. L. Villanueva et al., manuscript in preparation, 2011).

[46] The C_2H_6 production rate for W1 at 79 K is $(2.35 \pm 0.02) \times 10^{26} mol s^{-1}$. For the three comets, we measured E_g/A_g ratios to be consistent with equilibrium ($T_{spin} > 10 K$).

[47] As shown in Figures 12–15, the new model shows excellent line-by-line agreement with the cometary data sets, ultimately allowing us to extract improved cometary abundances (Tables 3 and 4). The new model has also led to improved understanding of this complex spectral region, where many other hydrocarbons have strong spectral signatures (e.g., methanol [CH_3OH], methane [CH_4], ethylene [C_2H_4]).

[48] The improvement of the C_2H_6 fluorescence model is attributed to differences between the old [Dello-Russo et al.,

Table 3. Fluxes and Production Rates (Q) for 7 Q Subbranches of the ν_7 Band of C_2H_6

ID	Frequency ^a (cm ⁻¹)	E_{rot} (cm ⁻¹)	g Factor ^b × 10 ⁻⁵ (s ⁻¹)	Transmittances	TOA Flux ^c × 10 ⁻¹⁸ (W m ⁻²)		Production Rate × 10 ²⁶ (s ⁻¹)	
					Flux	Sigma	Q	Sigma
<i>Comet C/2007 W1 (Boattini) – $T_{rot} = 79 K$</i>								
^R Q ₄	3000.2124	90.81	1.58545	0.8666	1.0369	0.0250	2.3613	0.0569
^R Q ₂	2993.4586	73.30	2.55965	0.9100	1.6418	0.0244	2.3210	0.0345
^R Q ₁	2990.0776	63.13	3.07130	0.8132	2.0151	0.0256	2.3770	0.0301
^R Q ₀	2986.7182	56.56	3.97371	0.9453	2.6096	0.0204	2.3818	0.0186
^P Q ₁	2983.3840	58.10	3.06727	0.9581	1.9262	0.0212	2.2802	0.0250
^P Q ₂	2980.0774	67.43	2.58050	0.7873	1.7046	0.0267	2.4011	0.0375
^P Q ₃	2976.7854	81.82	2.19640	0.9491	1.4041	0.0242	2.3263	0.0401
Weighted Mean							2.3513	0.0173
<i>Comet C/2004 Q2 (Machholz) – $T_{rot} = 93 K$</i>								
^R Q ₄	3000.2230	108.50	1.62755	0.8664	4.0881	0.0623	12.835	0.1955
^R Q ₂	2993.4579	84.47	2.44481	0.7769	6.1209	0.0719	12.822	0.1506
^R Q ₁	2990.0752	75.42	2.85883	0.7882	7.4671	0.0604	13.392	0.1082
^R Q ₀	2986.7144	69.13	3.65410	0.8820	10.148	0.0643	14.256	0.0903
^P Q ₁	2983.3840	69.34	2.84345	0.8796	7.1421	0.0498	12.907	0.0900
^P Q ₂	2980.0768	78.37	2.45732	0.7311	6.3405	0.1423	13.274	0.2979
^P Q ₃	2976.7883	93.62	2.18030	0.9213	5.3157	0.0585	12.556	0.1381
Weighted Mean							13.309	0.2514
<i>Comet 8P/Tuttle – $T_{rot} = 60 K$</i>								
^R Q ₄	3000.2855	100.18	0.95049	0.9095	0.2265	0.0406	1.6573	0.2969
^R Q ₁	2990.0819	49.10	3.29522	0.7555	0.8215	0.0686	1.7396	0.1452
^R Q ₀	2986.7192	42.09	4.48408	0.8769	1.1869	0.0468	1.8490	0.0729
^P Q ₁	2983.3820	44.73	3.36980	0.9115	0.7589	0.0425	1.5749	0.0882
^P Q ₂	2980.0731	51.61	2.69160	0.7414	0.6785	0.0624	1.7649	0.1622
Weighted Mean							1.7383	0.0594

^aRest frequency is the weighted mean of the frequencies composing each Q branch, where the weight is the g factor times transmittance for each compounding line.

^bIntegrated fluorescence efficiencies in the spectral region of the corresponding Q branch from the new model synthesized with the appropriate rotational temperatures and heliocentric velocities –8P/Tuttle: $T_{rot} = 60$ K and $\nu_h = -0.37$ km s⁻¹, C/2007 W1: $T_{rot} = 79$ K and $\nu_h = +9.70$ km s⁻¹, C/2004 Q2: $T_{rot} = 93$ K and $\nu_h = -2.01$ km s⁻¹.

^cTotal transmittance-corrected flux considering a 0.432 × 1.782 arcsec² box for the W1 and Q2 results (NIRSPEC) and 0.400 × 1.29 arcsec² for the 8P results (CRIRES).

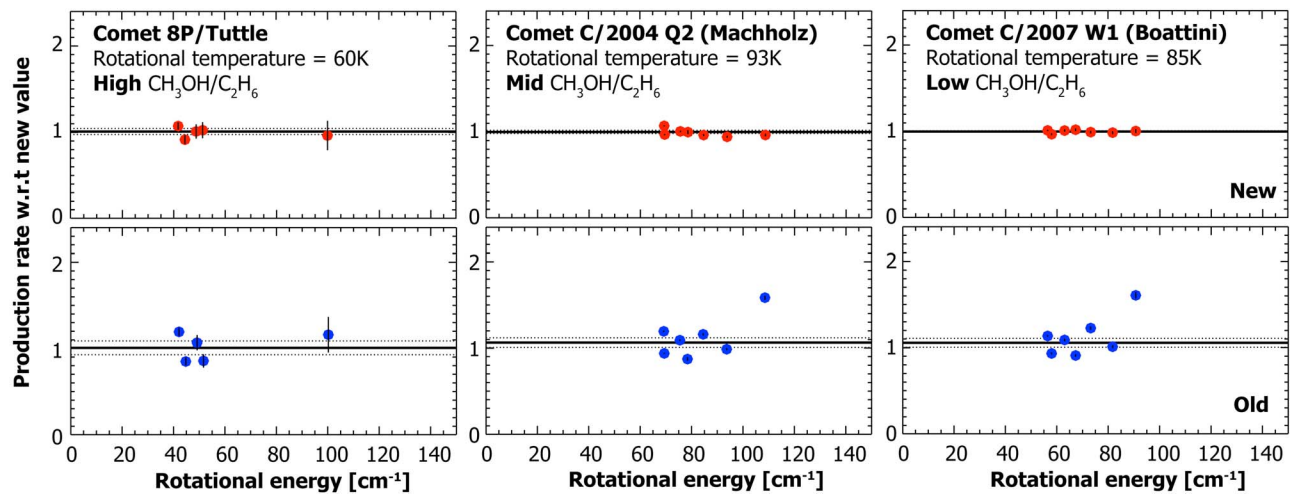


Figure 15. Excitation diagrams showing total production rates retrieved from individual ethane Q sub-branches, based on the new (Table 3) and old models. Results considering the new model are shown relative to the “new” mean in the upper panels, while the “old” results are presented in the lower panels.

Table 4. Measured Ethane Abundance in Selected Planetary and Cometary Atmospheres

Atmosphere	Abundance Relative to Standard Profile ^a	Ethane (C_2H_6) Mixing Ratios ^a
<i>Mars: Ethane (C_2H_6) Search^b</i>		
62°N–62°S, 295°W–308°W at $L_s = 323^\circ$ (MY 29), 18 August 2009		<0.8 ppb (3 σ)
41°N–76°S, 57°W–67°W at $L_s = 352^\circ$ (MY 27), 6 January 2006		<1.5 ppb (3 σ)
<i>Earth: Ethane (C_2H_6) Surface Level Volume Mixing Ratio^a</i>		
Mauna Kea (4200 m, Hawaii), 6 January 2006	0.49 ± 0.03	(0.97 ± 0.06) ppb
Paranal (2635 m, Chile), 18 August 2009	0.15 ± 0.02	(0.30 ± 0.04) ppb
<i>Comets: Ethane (C_2H_6) Abundance Relative to Water (H_2O)^c</i>		
C/2007 W1 (Boattini), 9 July 2008, NIRSPEC at Keck II		(1.957 ± 0.053) %
C/2004 Q2 (Machholz), 19 January 2005, NIRSPEC at Keck II		(0.488 ± 0.016) %
8P/Tuttle, 26 January 2008, CRIRES at VLT		(0.291 ± 0.017) %

^aAssuming the “standard” Northern Hemisphere vertical profile as presented in Figure 8c, we retrieved the scaling factor presented. A value of 0.15 (1/7) is consistent with the findings of *Helmlig et al.* [2009] for the Southern Hemisphere. The value for Mauna Kea is similar to the findings of *Rinsland et al.* [1994] for Mauna Loa at this season (corrected for hot-band absorption; see text).

^bMars: We searched for ethane at seven latitudinal intervals along the central meridian in August 2009 and January 2006, achieving extremely high sensitivities. The spectra presented in Figures 9 and 10 also sample the methane P branch, allowing us to obtain in January 2006 a sensitive upper limit for CH_4 of <8 ppb (3 σ) (consistent with *Mumma et al.* [2009]). The data taken with CRIRES in August 2009 were test exposures, and the Doppler shift (-9.4 km s $^{-1}$) was not sufficient to search for CH_4 on Mars.

^cThe ethane mixing ratios in comets are defined with respect to water, the main volatile constituent.

2001] and new models arising from four aspects: (1) the previous model did not properly account for the symmetries of ℓ splitting of rotational levels of the ν_7 vibrational level, leading to incorrect rovibrational branching ratios; (2) we introduced updated molecular constants, partition functions, and performed a line-by-line analysis (instead of a temperature independent “ g -band” analysis); (3) we included the complete fine rotational structure (P , Q , and R branches) of the ν_7 band (including hot bands), leading to an overall increase in the considered flux integrated within each Q branch; and (4) the new model considers a realistic solar pumping spectrum.

6. Conclusions

[49] We constructed a line-by-line model for the ν_7 band of ethane (C_2H_6), applying it to compute telluric transmittances and cometary fluorescence efficiencies. The complex and dense rotational fine structure of the ν_7 band system was described using a set of accurate rotational constants for each K ladder, including torsional hot bands. The new band sys-

tems were integrated into an advanced radiative transfer model of the terrestrial atmosphere (LBLRTM), considering a rigorous line-by-line, layer-by-layer radiative transfer analysis and including realistic atmospheric conditions, abundance profiles, and geometric conditions. In addition to adding 17,266 ethane lines (ν_7 and $\nu_7 + \nu_4 - \nu_4$) to the spectral database accessed by the terrestrial model, we updated and expanded the CO_2 database by including our latest discoveries in the Martian atmosphere. Using these new models, we achieved excellent agreement with transmittance and fluorescence emission data recorded near 3.3 μ m using three different instruments located in the Northern and Southern hemispheres.

[50] We computed cometary fluorescence emission rates for a wide range of rotational temperatures (10 K–200 K) and validated the model by comparing it to measured spectra of three comets (C/2007 W1 (Boattini), C/2004 Q2 (Machholz), and 8P/Tuttle). The model makes use of a novel approach to synthesize the solar pumping, which combines a theoretical continuum model and a highly precise solar line list. The methodology used to calculate cometary fluorescence emis-

Table A1. Carbon Dioxide (CO_2) Rovibrational Constants and Band Strengths^a

Level	G_v (cm $^{-1}$)	B_v (cm $^{-1}$)	D_v (cm $^{-1}$) $\times 10^{-7}$	H_v (cm $^{-1}$) $\times 10^{-13}$	S_v^0 (cm $^{-1}$ / mol cm $^{-2}$) $\times 10^{-25}$	$a1$
$^{16}O^{12}C^{18}O$ (CO_2 628) ^b						
00001	0.0	0.36818450	1.18647	-0.150		
01111e	2982.11105	0.36573112	1.20268	0.217	1.83	-0.003
01111f		0.36626757	1.20380*	-0.296*		
$^{16}O^{12}C^{17}O$ (CO_2 627) ^c						
00001	0.0	0.37861462	1.26428	0.000		
20001	2775.58690	0.37931621	1.48387	0.000	2.14	
$^{16}O^{13}C^{18}O$ (CO_2 638) ^d						
00001	0.0	0.36818116	1.18498	0.000		
20001	2701.932484	0.36833043	0.872951	0.000	0.53	

^aBand strengths are for transitions from the ground level and an excitation temperature of 296 K. Value “ $a1$ ” is the first Herman-Wallis coefficient [*Rothman et al.*, 1992, equation 14].

^b*Villanueva et al.* [2008a] and *Rothman et al.* [1992].

^c*Villanueva et al.* [2008b] and *Rothman et al.* [1992].

^d*Villanueva et al.* [2008b], *Vandaele et al.* [2009], and *Rothman et al.* [1992].

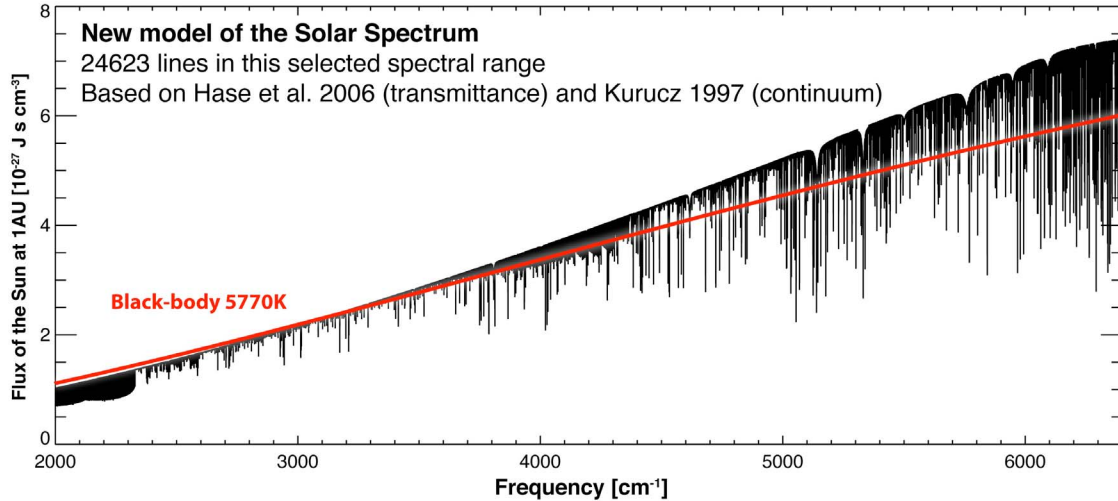


Figure B1. Spectrum of the Sun in the near-infrared region ($1.6\text{--}5\ \mu\text{m}$) based on a theoretical model for the continuum (see combined Web/outgoing-FTP site, <http://kurucz.harvard.edu/>) and a new solar line list [Hase *et al.*, 2006]. The red trace shows the continuum of a blackbody at 5770 K.

sion rates was standardized to extract information from spectral databases on C_2H_6 and all other molecules in the HITRAN database; thus, it is readily available to compute cometary fluorescence emission rates for multiple other molecules.

Appendix A: HITRAN Corrections and Updates

[51] We use the universally recognized HITRAN database as the base for our radiative transfer model (using LBLRTM) and include our own corrections and updates. To the HITRAN 2008 release, we (1) applied the current updates available on the HITRAN Web site (<http://www.cfa.harvard.edu/hitran/updates.html>), (2) added our new model for the ν_7 and $\nu_7 + \nu_4 - \nu_4$ bands of C_2H_6 (17,266 spectral lines), and (3) expanded the CO_2 database to include our latest discoveries in the Martian atmosphere (1780 lines of four bands).

[52] We recently discovered multiple unknown isotopic bands of CO_2 not previously described in the refereed literature (and not present in the HITRAN atlas) when analyzing spectra of CO_2 -rich Mars [Villanueva *et al.*, 2008a, 2008b]. The observations were performed using high-resolution Echelle spectrometers, allowing us to extract precise spectroscopic constants for the levels involved [see Villanueva *et al.*, 2008b, Table 1] for the $\nu_2 + \nu_3$ band of $^{16}\text{O}^{12}\text{C}^{18}\text{O}$ at $3.3\ \mu\text{m}$, the $2\nu_1$ band of $^{16}\text{O}^{12}\text{C}^{17}\text{O}$ at $3.6\ \mu\text{m}$, and the $2\nu_1$ band of the rare isotope $^{16}\text{O}^{13}\text{C}^{18}\text{O}$ at $3.7\ \mu\text{m}$. In a follow-up study by the Venus Express SOIR Team, our detection of $2\nu_1$ ($^{16}\text{O}^{13}\text{C}^{18}\text{O}$) band was confirmed, and they have recently retrieved an improved set of spectroscopic constants for this band [Vandaele *et al.*, 2009]. A compilation of all constants is presented in Table A1.

Appendix B: Solar Spectrum

[53] We created a high-resolution flux-calibrated solar spectrum by combining an empirical line-by-line model for the infrared solar transmittance [Hase *et al.*, 2006] with a purely theoretical model for the solar continuum irradiance

(see combined Web/outgoing-FTP site, <http://kurucz.harvard.edu/>) (Figure B1). Knowledge of the solar spectrum has greatly improved in the past few decades due to spacecraft measurements (ATMOS mission [Abrams *et al.*, 1996], ACE instrument [Hase *et al.*, 2010]), and the comprehensive solar survey performed at the McMath-Pierce telescope at the Kitt-Peak National Observatory [Wallace and Livingston, 2003]. One of the biggest limitations of these databases is that they are not flux calibrated, and the spectra can only be used to extract transmittance information. However, theoretical models have been extremely successful in calculating a flux-calibrated solar continuum, but their prediction of solar spectral features is still not optimum. There are several theoretical solar models [e.g., Tobiska *et al.*, 2000]. The Kurucz (see combined Web/outgoing-FTP site, <http://kurucz.harvard.edu/>) solar irradiance spectrum is considered best when averaged to (nm) resolutions [Fiorenza and Formisano, 2005], but it does not describe the spectral morphology precisely (Figure B2). In the case of the flux-calibrated solar spectrum presented by Fiorenza and Formisano [2005], we could not reproduce their reported values, and we suspect of an incorrect labeling of their flux units.

[54] Using the ATMOS spectrum and other ground-based measurements of the Sun, Hase *et al.* [2006] generated an empirical line-by-line list model of the solar transmittance spectrum. Recently, the same group has constructed a highly sensitive infrared solar spectrum from ACE-FTS observations [Hase *et al.*, 2010], and they were able to assign numerous weak absorption features (that were not detectable in the ATMOS solar observations) due to the improved SNR of the ACE-FTS data. However, Hase *et al.* [2010] did not create line-by-line empirical data, only solar transmittance as a function of frequency.

[55] The solar line list of Hase *et al.* [2006] includes intensities and identifications for each line and a parameterization of the lineshape (Gaussian $w = 0$, Lorentzian $w = 1$). It also accounts for center-to-limb variation of lines and continuum brightness temperature. In addition, the synthetic spectrum generated in this manner has a much greater signal-

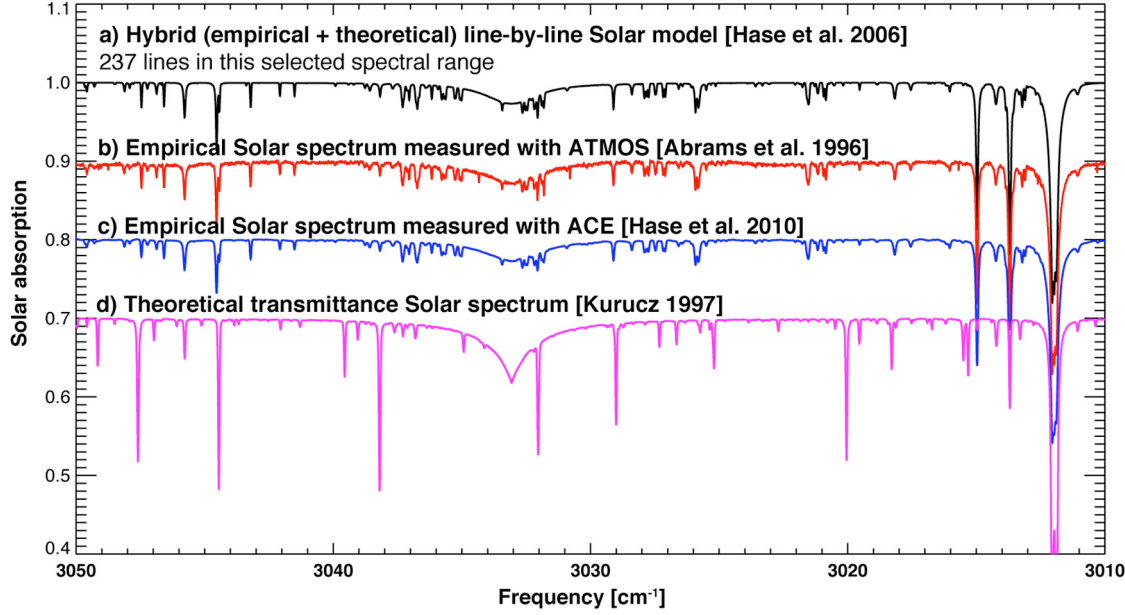


Figure B2. Comparison of measured and synthetic solar spectra. (a) Synthesized spectrum adopting 237 solar lines listed in the *Hase et al.* [2006] atlas and using four parameters per line (center, strength, width, and shape parameter). Solar spectrum as measured (b) with ATMOS instrument from space shuttle and (c) with ACE instrument onboard SCISAT-1. (d) Spectrum modeled by *Kurucz* (see combined Web/outgoing-FTP site, <http://kurucz.harvard.edu/>), with spectral lines included; it clearly does not reproduce the observed spectra (Figures B2b and B2c). For clarity purposes, Figure B2 was shifted vertically by -0.1 (Figure B2b), -0.2 (Figure B2c), and -0.3 (Figure B2d).

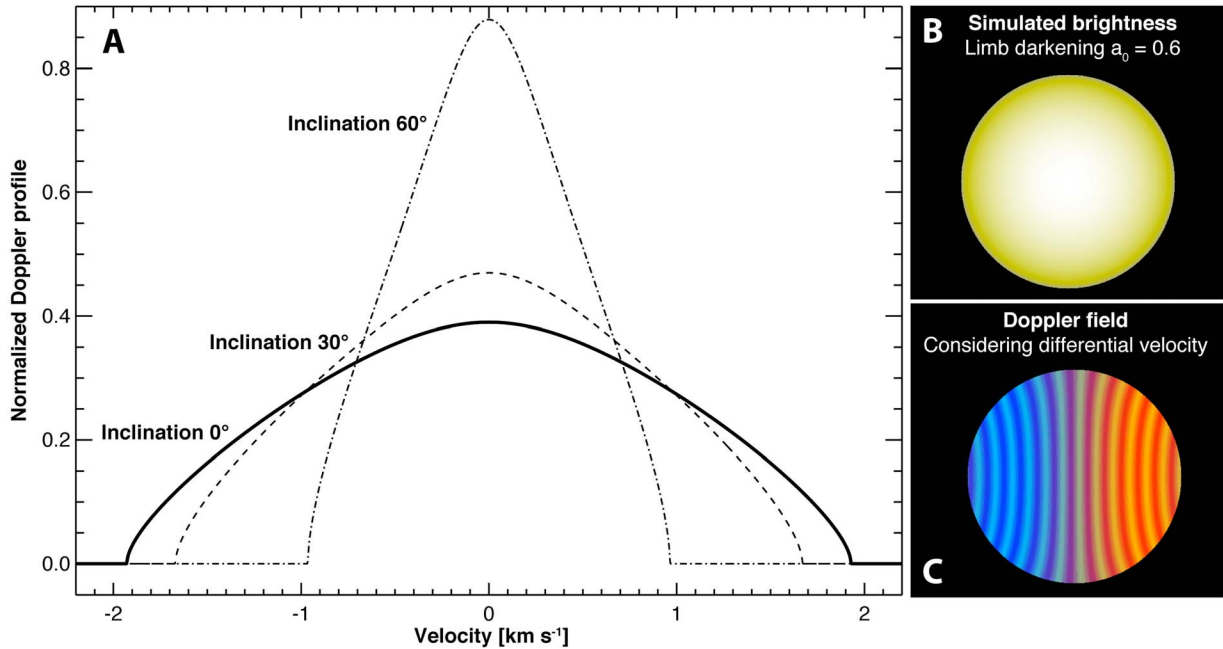


Figure B3. (a) Solar rotation kernels for different inclinations relative to the rotation plane. These profiles are used to transform synthetic disk-center spectra by *Hase et al.* [2006] to disk-integrated spectra at different inclinations in the solar system. (b) Simulated line intensity considered a limb darkening coefficient a_0 of 0.6. (c) Doppler field computed adopting a latitude differential velocity profile using coefficients retrieved from Doppler measurements [*Snodgrass and Ulrich*, 1990]. Blue indicates motion toward the observer, whereas red indicates motions away from the observer. Yellow vertical lines are traces of iso-velocity.

to-noise ratio since each line can be properly described by just four line parameters. By multiplying this realistic transmittance spectrum of *Hase et al.* [2006] with the highly accurate continuum model of *Kurucz* (see combined Web/outgoing-FTP site, <http://kurucz.harvard.edu/>), we generated a flux-calibrated solar spectrum in the wavelength range 700–6400 cm⁻¹ (Figure B1). We simulate the integrated disk spectrum by convolving the synthetic spectra with a solar rotation line profile, which includes differential rotation (A: 14.713 deg/day, B: -2.396 deg/day, C: -1.787 deg/day) [Snodgrass and Ulrich, 1990], limb darkening ($u = 0.6$), and the capability to compute integrated disk spectra for different inclinations (Figure B3). At the ecliptic, the broadening by this effect is ~ 2.5 km s⁻¹ (FWHM). This approximation is far from optimum, but it provides an intermediate solution until a line list for the integrated disk at different inclinations becomes available. This spectrum was used to compute the fluorescence pumping in equation (C.3). In Figure B2, we show a comparison between the spacecraft solar spectrum measured by the ATMOS instrument [Abrams et al., 1996], the empirical line-by-line solar model using ATMOS data [Hase et al., 2006], the solar spectrum of *Hase et al.* [2010] using ACE-FTS data, and the theoretical solar irradiance spectrum by *Kurucz* (see combined Web/outgoing-FTP site, <http://kurucz.harvard.edu/>).

Appendix C: General Fluorescence Model

[56] We require 11 parameters from the HITRAN database to compute g factors: molecular identification (M), isotopologue number (I), frequency of the transition (ν (cm⁻¹)), Einstein A coefficient (A_{21} (s⁻¹)), lower-state energy (E'' (cm⁻¹)), upper and lower global vibrational quantum numbers (V , V''), upper and lower local rotational quantum numbers (L' , L''), and upper and lower statistical weights (w' , w''). (To avoid confusing fluorescence emission rates (g factors) with statistical weights, we use the letter ‘ w ’ (instead of the standard terminology, ‘ g ’) to refer to the latter.) Even though Einstein A coefficients can be computed from absorption line intensities [Šimečková et al., 2006], the inclusion of A coefficients in HITRAN since 2004 (which replaced the weighted square of the transition moment) has been a great advance, and is of significant value to studies related to non-LTE processes.

[57] In computing line-by-line fluorescence efficiencies (g factors), we need to build a full quantum mechanical model for a molecular band. We illustrate that process for C₂H₆. In the following sections, we present how we (a) create the rovibrational structure of the energy levels, (b) compute the total partition function (Q_{tot}), (c) calculate pumping rates, and (d) calculate emission rates.

C1. Re-creation of Rovibrational Energy Levels

[58] The rovibrational structure of the energy levels involved in a particular band system can be straightforwardly retrieved from the information of the individual lines in the HITRAN database. For example, by isolating lines from a defined band, and using six parameters (ν , E'' , L' , L'' , w' , w'') for each line, we can recreate an indexed rotational structure (energy) of the lower and upper states: $E''(L'') = Ei''$; $E'(L') = Ei' + \nu$, where i is the line index, and L' and L'' refer to the

local quantum numbers for the levels that is determined by the rotational structure. For linear molecules such as CO (carbon monoxide) and C₂H₂ (acetylene), the local quantum number is described by a single value ($L = J$, where J is the total angular momentum); for symmetric tops, $L = (J, K, \ell)$ (e.g., C₂H₆); and for molecules such as HDO (a prolate asymmetric top), the structure is stored in a $E(J, K_a, K_c)$ array, and the local quantum numbers would be $L = (J, K_a, K_c)$.

C2. Computation of Partition Function

[59] Computation of the total partition function (Q_{tot}) is particularly difficult, requiring complete knowledge of all electronic, vibrational, and rotational modes. In the seminal paper by *Gamache et al.* [1990], this problem was addressed for a limited set of linear molecules in the 70 K–3000 K range; the first step in the development of the now widely used TIPS program. This study has now been extended to the full database, and currently the HITRAN database provides total partition sums for all molecules and isotopologues present in the database for the 70 K–3000 K temperature range [Goldman et al., 2000; Fischer et al., 2003; Pine and Rinsland, 1999].

[60] For temperatures lower than 70 K, we have considered an analytical approach where we compute the vibrational and rotational partition functions independently. By using the retrieved rotational structure, we compute the rotational partition function as:

$$Q_r = \sum_{i=L_{\min}}^{L_{\max}} w_i'' \exp(-c_2 E_i''/T). \quad (C1)$$

For most molecules (not C₂H₆), the vibrational partition function for temperatures lower than 70 K can be assumed to be unity since they are only populated in their lowest vibrational/electronic level, and herewith the total partition function can be approximated to $Q_{tot} = Q_e Q_v Q_r \sim Q_r$ for low temperatures. In the case of C₂H₆ with a low-energy vibrational level at ~ 289 cm⁻¹ ($E\nu_4$, torsional mode), we computed the vibrational partition for temperatures lower than 70 K as following:

$$Q_{vib} = [1 - \exp(-c_2 E\nu_4/T)]^{-1}. \quad (C2)$$

C3. Computation of Fluorescence Pumping Rates

[61] Perhaps one of the most valuable elements of spectral line lists is that the selection rules are explicitly defined by the existence (or nonexistence) of a line. In addition, Hönl-London factors and Herman-Wallis effects (which are molecule and band dependent) are directly contained in the line intensities and A coefficients. By iterating through the line atlas for each line, we compute the pumping rate (g_{pump} (s⁻¹)) from the reported A coefficient (A_{21}), and add it to the corresponding upper-state population defined in $L'(J', \dots)$ following [Crovisier and Encrenaz, 1983; Weaver and Mumma, 1984; Šimečková et al. 2006]:

$$g_{pump}(L') = \sum J_s(v_s) \cdot B_{12} \cdot w'' \exp(-c_2 E''/T) / Q_{tot}(T) \quad (C3)$$

$$A_{tot}(L') = \sum A_{21} \quad (C4)$$

$$B_{12} = B_{21} \cdot \frac{w'}{w''} \quad (C5)$$

$$B_{21} = A_{21} \cdot (8\pi h v^3)^{-1} \quad (C6)$$

$$v_s = (1 - u/c)v, \quad (C7)$$

where J_s is the solar flux (J s cm^{-3}) see Appendix B) at the Doppler-shifted frequency v_s of the line (being u (cm s^{-1}) the relative velocity between the comet and the Sun and c the speed of light (cm s^{-1})), B_{12} , the Einstein coefficient for induced absorption ($\text{J}^{-1} \text{s}^{-2} \text{cm}^3$), B_{21} , the Einstein coefficient for stimulated emission ($\text{J}^{-1} \text{s}^{-2} \text{cm}^3$), A_{tot} , the sum of Einstein A coefficients (s^{-1}) mapping to the upper state, and h Planck's constant (J s).

C4. Computation of Fluorescence Emission Rates

[62] Once all pumps are computed, the branching ratios for each line ' i ' are calculated as A_{21}/A_{tot} , and with this cometary fluorescence rates (g factor) are calculated as:

$$g_i = g_{pump}(L') \cdot \frac{A_{21}}{A_{tot}(L')} \quad (C8)$$

[63] Even though the branching ratios (A_{21}/A_{tot}) are temperature independent, the line-by-line pumping rates (g_{pump}) are not; thus, g factors must be computed for every line at the appropriate temperature.

[64] **Acknowledgments.** G.L.V. acknowledges support from NASA's Planetary Astronomy Program (08-PAST08-0034) and Planetary Atmospheres Program (08-PATM08-0031). M.J.M. was supported by NASA's Planetary Astronomy Program (RTOP 344-32-07) and Astrobiology Program (RTOP 344-53-51). K.M.S. was supported by the Planetary Astronomy RUI program of the National Science Foundation. We thank Hans-Ulrich Käufl for assisting with the Mars (CRIRES) observations in 2009, and Robert Novak and Avram M. Mandell for assisting with the acquisition of Mars (CSHELL) data in 2006. We thank the staff at the VLT Observatory (operated by ESO), W.M. Keck Observatory (operated as a scientific partnership among Caltech, UCLA, and NASA), and NASA's InfraRed Telescope Facility (operated for NASA by the University of Hawaii) for their exceptional support throughout our long Mars and cometary observing programs. The authors want to recognize and acknowledge the significant cultural role and reverence that the summit of Mauna Kea has always had within the indigenous Hawaiian community. We are most fortunate to have the opportunity to conduct observations from this mountain.

References

- Abrams, M. C., A. Goldman, M. R. Gunson, C. P. Rinsland, and R. Zander (1996), Observations of the infrared solar spectrum from space by the ATMOS experiment, *Appl. Opt.*, 35, 2747, doi:10.1364/AO.35.002747.
- Anderson, G. P., S. A. Clough, F. X. Kneizys, J. H. Chetwynd, and E. P. Shettle (1986), *AFGL Atmospheric Constituent Profiles (0–120 km)*, *Tech. Rep. 86-0110*, 43 pp., Air Force Geophys. Lab., Hanscom AFB, Mass.
- Blass, W. E., G. W. Halsey, J. Susskind, D. C. Reuter, and D. E. Jennings (1990), Rotational parameters of the first torsional state of ethane from lower state combination differences in $\nu_9 + \nu_4 - \nu_4$, *J. Mol. Spectrosc.*, 141, 334, doi:10.1016/0022-2852(90)90170-U.
- Böhnhardt, H., M. J. Mumma, G. L. Villanueva, M. A. DiSanti, B. P. Bonev, M. Lippi, and H. U. Käufl (2008), The unusual volatile composition of the Halley-type comet 8P/Tuttle: Addressing the existence of an inner Oort cloud, *Astrophys. J.*, 683, L71, doi:10.1086/591446.
- Bonev, B. P., M. J. Mumma, E. L. Gibb, M. A. DiSanti, G. L. Villanueva, K. Magee-Sauer, and R. S. Ellis (2009), Comet C/2004 Q2(Machholz): Parent volatiles, a search for deuterated methane, and constraint on the CH₄ spin temperature, *Astrophys. J.*, 699, 1563, doi:10.1088/0004-637X/699/2/1563.
- Brown, L. R., C. B. Farmer, C. P. Rinsland, and R. A. Toth (1987), Molecular line parameters for the Atmospheric Trace Molecule Spectroscopy (ATMOS) experiment, *Appl. Opt.*, 26, 5154.
- Clough, S. A., M. W. Shephard, E. J. Mlawer, J. S. Delamere, M. J. Iacono, K. Cady-Pereira, S. Boukabara, and P. D. Brown (2005), Atmospheric radiative transfer modeling: A summary of the AER codes, *J. Quant. Spectrosc. Radiat. Transf.*, 91, 233, doi:10.1016/j.jqsrt.2004.05.058.
- Cole, A. R. H., K. J. Cross, J. A. Cugley, and H. M. Heise (1980), Infrared rotation-vibration spectra of ethane: The perpendicular band ν_7 of C₂H₆, *J. Mol. Spectrosc.*, 83, 233, doi:10.1016/0022-2852(80)90047-8.
- Crovisier, J., and T. Encrenaz (1983), Infrared fluorescence of molecules in comets: The general synthetic spectrum, *Astron. Astrophys.*, 126, 170.
- Dang-Nhu, M., and A. Goldman (1987), Line parameters for C₂H₆ in the 3000 cm⁻¹ region, *J. Quant. Spectrosc. Radiat. Transf.*, 38, 159, doi:10.1016/0022-4073(87)90041-0.
- Dang-Nhu, M., A. S. Pine, and W. J. Lafferty (1984), Intensities in the ν_5 , ν_7 , and $\nu_8 + \nu_{11}$ bands of ethane ¹²C₂H₆, *Can. J. Phys.*, 62, 512, doi:10.1139/p84-069.
- Dello Russo, N., M. J. Mumma, M. A. DiSanti, K. Magee-Sauer, and R. Novak (2001), Ethane production and release in comet C/1995 O1 Hale-Bopp, *Icarus*, 153, 162, doi:10.1006/icar.2001.6678.
- Dello Russo, N., M. J. Mumma, M. A. DiSanti, K. Magee-Sauer, E. L. Gibb, B. P. Bonev, I. S. McLean, and L. Xu (2006), A high-resolution infrared spectral survey of comet C/1999 H1 Lee, *Icarus*, 184, 255, doi:10.1016/j.icarus.2006.04.020.
- DiSanti, M. A., and M. J. Mumma (2008), Reservoirs for comets: Compositional differences based on infrared observations, *Space Sci. Rev.*, 138, 127, doi:10.1007/s11214-008-9361-0.
- Edwards, D. P. (1992), *GENLN2: A General Line-by-Line Atmospheric Transmittance and Radiance Model, Version 3.0, Description and Users' Guide*, NCAR/TN-367-STR, Natl. Cent. for Atmos. Res., Boulder, Colo.
- Fernández, J. M., and S. Montero (2003), Torsional selection rules, Raman tensors, and cross sections for degenerate modes of C₂H₆, *J. Chem. Phys.*, 118, 2657, doi:10.1063/1.1535420.
- Fiorenza, C., and V. Formisano (2005), A solar spectrum for PFS data analysis, *Planet. Space Sci.*, 53, 1009, doi:10.1016/j.pss.2004.12.008.
- Fischer, J., R. R. Gamache, A. Goldman, L. S. Rothman, and A. Perrin (2003), Total internal partitions sums for molecular species on the 2000 edition of the HITRAN database, *J. Quant. Spectrosc. Radiat. Transf.*, 82, 401, doi:10.1016/S0022-4073(03)00166-3.
- Gamache, R. R., R. L. Hawkins, and L. S. Rothman (1990), Total internal partition sums in the temperature range 70–3000 K: Atmospheric linear molecules, *J. Mol. Spectrosc.*, 142, 205, doi:10.1016/0022-2852(90)90178-S.
- Glatthor, N., T. von Clarmann, G. P. Stiller, B. Funke, M. E. Koukouli, H. Fischer, U. Grabowski, M. Höpfner, S. Kellmann, and A. Linden (2009), Large-scale upper tropospheric pollution observed by MIPAS HCN and C₂H₆ global distributions, *Atmos. Chem. Phys.*, 9, 9619, doi:10.5194/acp-9-9619-2009.
- Goldman, A., M. Dang-Nhu, and J. P. Bouanich (1989), Ethane 3 μm spectral clusters of atmospheric interest, *J. Quant. Spectrosc. Radiat. Transf.*, 41, 17, doi:10.1016/0022-4073(89)90016-2.
- Goldman, A., R. R. Gamache, A. Perrin, J. M. Flaud, C. P. Rinsland, and L. S. Rothman (2000), HITRAN partition function and weighted transition-moments squared, *J. Quant. Spectrosc. Radiat. Transf.*, 66, 455, doi:10.1016/S0022-4073(99)00176-4.
- Harrison, J. J., N. D. C. Allen, and P. F. Bernath (2010), Infrared absorption cross sections for ethane (C₂H₆) in the 3 μm region, *J. Quant. Spectrosc. Radiat. Transf.*, 111, 357, doi:10.1016/j.jqsrt.2009.09.010.
- Hase, F., P. Demoulin, A. J. Sauval, G. C. Toon, P. F. Bernath, A. Goldman, J. W. Hannigan, and C. P. Rinsland (2006), An empirical line-by-line model for the infrared solar transmittance spectrum from 700 to 5000 cm⁻¹, *J. Quant. Spectrosc. Radiat. Transf.*, 102, 450, doi:10.1016/j.jqsrt.2006.02.026.
- Hase, F., L. Wallace, S. D. Mcleod, J. J. Harrison, and P. F. Bernath (2010), The ACE-FTS atlas of the infrared solar spectrum, *J. Quant. Spectrosc. Radiat. Transf.*, 111, 521, doi:10.1016/j.jqsrt.2009.10.020.
- Helmlig, D., J. Bottenheim, I. E. Galbally, A. Lewis, M. J. T. Milton, S. Penkett, C. Plass-Duelmer, S. Reimann, P. Tans, and S. Thiel (2009), Volatile organic compounds in the global atmosphere, *Eos Trans. AGU*, 90, 513, doi:10.1029/2009EO520001.
- Herzberg, G. (1945), *Molecular Spectra and Molecular Structure: II. Infrared and Raman Spectra of Polyatomic Molecules*, Van Nostrand Reinhold, Princeton, N. J.
- Hough, A. M. (1991), Development of a two-dimensional global tropospheric model: Model chemistry, *J. Geophys. Res.*, 96(D4), 7325, doi:10.1029/90JD01327.

- Hougen, J. T. (2005), CHEMISTRY: Nuclear spin conversion in molecules, *Science*, **310**, 1913–1914, doi:10.1126/science.1122110.
- Käufl, H., et al. (2004), CRIRES: A high-resolution infrared spectrograph for ESO's VLT: Ground-based instrumentation for astronomy, *Proc. SPIE Int. Soc. Opt. Eng.*, **5492**, 12.
- Kunde, V. R., and W. C. Maguire (1974), Direct integration transmittance model, *J. Quant. Spectrosc. Radiat. Transf.*, **14**, 803, doi:10.1016/0022-4073(74)90124-1.
- Malathy Devi, V., D. C. Benner, C. P. Rinsland, M. A. H. Smith, R. L. Sams, T. A. Blake, J. Flaud, K. Sung, L. R. Brown, and A. W. Mantz (2010a), Multispectrum measurements of spectral line parameters including temperature dependences of N_2 - and self-broadened half-width coefficients in the region of the ν_9 band of $^{12}\text{C}_2\text{H}_6$, *J. Quant. Spectrosc. Radiat. Transf.*, **111**, 2481, doi:10.1016/j.jqsrt.2010.07.010.
- Malathy Devi, V., C. P. Rinsland, C. D. Benner, R. L. Sams, and T. A. Blake (2010b), Multispectrum analysis of the ν_9 band of $^{12}\text{C}_2\text{H}_6$: Positions, intensities, self- and N_2 -broadened half-width coefficients, *J. Quant. Spectrosc. Radiat. Transf.*, **111**, 1234, doi:10.1016/j.jqsrt.2009.10.017.
- McLean, I. S., et al. (1998), Design and development of NIRSPEC: A near-infrared Echelle spectrograph for the Keck II telescope, *Proc. SPIE Int. Soc. Opt. Eng.*, **3354**, 566.
- Mumma, M. J., and S. B. Charnley (2011), The chemical composition of comets—Natal heritage and emerging taxonomies, *Annu. Rev. Astron. Astrophys.*, in press.
- Mumma, M. J., M. A. DiSanti, N. D. Dello Russo, M. Fomenkova, K. Magee-Sauer, C. D. Kaminski, and D. X. Xie (1996), Detection of abundant ethane and methane, along with carbon monoxide and water, in comet C/1996 B2 Hyakutake: Evidence for interstellar origin, *Science*, **272**, 1310, doi:10.1126/science.272.5266.1310.
- Mumma, M. J., et al. (2001), A survey of organic volatile species in comet C/1999 H1(Lee) using NIRSPEC at the Keck Observatory, *Astrophys. J.*, **546**, 1183, doi:10.1086/318314.
- Mumma, M. J., G. L. Villanueva, R. E. Novak, T. Hewagama, B. P. Bonev, M. A. DiSanti, A. M. Mandell, and M. D. Smith (2009), Strong release of methane on Mars in northern summer 2003, *Science*, **323**, 1041–1045, doi:10.1126/science.1165243.
- Novak, R. E., M. J. Mumma, M. A. DiSanti, N. Dello Russo, and K. Magee-Sauer (2002), Mapping of ozone and water in the atmosphere of Mars near the 1997 Aphelion, *Icarus*, **158**, 14–23, doi:10.1006/icar.2002.6863.
- Oomens, J., and J. Reuss (1996), The $\nu_7 + \nu_9 - \nu_9$ hot band in ethane, *J. Mol. Spectrosc.*, **177**, 19, doi:10.1006/jmsp.1996.0112.
- Pine, A. S., and W. J. Lafferty (1982), Torsional splittings and assignments of the Doppler-limited spectrum of ethane in the C-H stretching region, *J. Res. Natl. Bur. Stand. U.S.*, **83**(3), 1.
- Pine, A. S., and C. P. Rinsland (1999), The role of torsional hot bands in modeling atmospheric ethane, *J. Quant. Spectrosc. Radiat. Transf.*, **62**, 445, doi:10.1016/S0022-4073(98)00114-9.
- Pine, A. S., and S. C. Stone (1996), Torsional tunneling and A_1 - A_2 splittings and air broadening of the RQ_0 and PQ_3 subbranches of the ν_7 band of ethane, *J. Mol. Spectrosc.*, **175**, 21, doi:10.1006/jmsp.1996.0004.
- Radeva, Y. L., M. J. Mumma, G. L. Villanueva, and M. F. A'Hearn (2011), A newly developed fluorescence model for C_2H_6 ν_5 and application to cometary spectra acquired with NIRSPEC at Keck II, *Astrophys. J.*, **729**, 135, doi:10.1088/0004-637X/729/2/135.
- Rinsland, C. P., A. Goldman, F. J. Murcay, S. J. David, R. D. Blatherwick, and D. G. Murcay (1994), Infrared spectroscopic measurements of the ethane (C_2H_6) total column abundance above Mauna Loa, Hawaii: Seasonal variations, *J. Quant. Spectrosc. Radiat. Transf.*, **52**, 273, doi:10.1016/0022-4073(94)90157-0.
- Rinsland, C. P., N. B. Jones, B. J. Connor, S. W. Wood, A. Goldman, T. M. Stephen, F. J. Murcay, L. S. Chiou, R. Zander, and E. Mahieu (2002), Multiyear infrared solar spectroscopic measurements of HCN, CO, C_2H_6 , and C_2H_2 tropospheric columns above Lauder, New Zealand (45°S latitude), *J. Geophys. Res.*, **107**(D14), 4185, doi:10.1029/2001JD001150.
- Rothman, L. S., R. L. Hawkins, R. B. Wattson, and R. R. Gamache (1992), Energy levels, intensities, and linewidths of atmospheric carbon dioxide bands, *J. Quant. Spectrosc. Radiat. Transf.*, **48**, 537, doi:10.1016/0022-4073(92)90119-O.
- Rothman, L. S., et al. (2009), The HITRAN 2008 molecular spectroscopic database, *J. Quant. Spectrosc. Radiat. Transf.*, **110**, 533, doi:10.1016/j.jqsrt.2009.02.013.
- Šimečková, M., D. Jacquemart, L. S. Rothman, R. R. Gamache, and A. Goldman (2006), Einstein A -coefficients and statistical weights for molecular absorption transitions in the HITRAN database, *J. Quant. Spectrosc. Radiat. Transf.*, **98**, 130, doi:10.1016/j.jqsrt.2005.07.003.
- Snodgrass, H. B., and R. K. Ulrich (1990), Rotation of Doppler features in the solar photosphere, *Astrophys. J.*, **351**, 309, doi:10.1086/168467.
- Sun, Z.-D. (2005), Separation and conversion dynamics of four nuclear spin isomers of ethylene, *Science*, **310**, 1938–1941, doi:10.1126/science.1120037.
- Tobiska, W. K., T. Woods, F. Eparvier, R. Viereck, L. Floyd, D. Bouwer, G. Rottman, and O. R. White (2000), The SOLAR2000 empirical solar irradiance model and forecast tool, *J. Atmos. Sol. Terr. Phys.*, **62**, 1233, doi:10.1016/S1364-6826(00)00070-5.
- Tokunaga, A. T., D. W. Toomey, J. Carr, D. N. B. Hall, and H. W. Epps (1990), Design for a 1–5 micron cryogenic Echelle spectrograph for the NASA IRTF, *Instrum. Astron. VII (Proc. SPIE)*, **1235**, 131, doi:10.1117/12.19082.
- Vandaele, A. C., et al. (2009), Updating CO_2 spectroscopic line list using Mars and Venus spectra, paper presented at International Conference on Comparative Planetology: Venus-Earth-Mars, *Eur. Space Agency*, Noordwijk, Netherlands, 11–15 May.
- Villanueva, G. L., M. J. Mumma, R. E. Novak, and T. Hewagama (2008a), Identification of a new band system of isotopic CO_2 near $3.3\text{ }\mu\text{m}$: Implications for remote sensing of biomarker gases on Mars, *Icarus*, **195**, 34, doi:10.1016/j.icarus.2007.11.014.
- Villanueva, G. L., M. J. Mumma, R. E. Novak, and T. Hewagama (2008b), Discovery of multiple bands of isotopic CO_2 in the prime spectral regions used when searching for CH_4 and HDO on Mars, *J. Quant. Spectrosc. Radiat. Transf.*, **109**, 883, doi:10.1016/j.jqsrt.2007.12.016.
- Wallace, L., and W. Livingston (2003), *An Atlas of the Solar Spectrum in the Infrared From 1850 to 9000 cm⁻¹ (1.1 to 5.4 microns)*, Tech. Rep. 03-001, Natl. Sol. Obs., Tucson, Ariz.
- Weaver, H. A., and M. J. Mumma (1984), Infrared molecular emissions from comets, *Astrophys. J.*, **276**, 782, doi:10.1086/161664.

K. Magee-Sauer, Department of Physics and Astronomy, Rowan University, Glassboro, NJ 08028, USA.

M. J. Mumma and G. L. Villanueva, Solar System Exploration Division, NASA Goddard Space Flight Center, Mailstop 690.3, Greenbelt, MD 20771, USA. (villanueva@nasa.gov)